

# The X-CLASS survey: A catalogue of 1646 X-ray-selected galaxy clusters up to $z \sim 1.5$

E. Koulouridis<sup>1</sup>, N. Clerc<sup>2</sup>, T. Sadibekova<sup>3</sup>, M. Chira<sup>1,4</sup>, E. Drigga<sup>1,4</sup>, L. Faccioli<sup>3</sup>, J. P. Le Fèvre<sup>3</sup>, C. Garrel<sup>3</sup>, E. Gaynullina<sup>5</sup>, A. Gkini<sup>1,6</sup>, M. Kosiba<sup>7,8</sup>, F. Pacaud<sup>9</sup>, M. Pierre<sup>3</sup>, J. Rüdiger<sup>10</sup>, K. Tazhenova<sup>3</sup>, C. Adami<sup>11</sup>, B. Altieri<sup>12</sup>, J.-C. Baguley<sup>13</sup>, R. Cabanac<sup>2</sup>, E. Cucchetti<sup>2</sup>, A. Khalikova<sup>5</sup>, M. Lieu<sup>14</sup>, J.-B. Melin<sup>15</sup>, M. Molham<sup>16</sup>, M. E. Ramos-Ceja<sup>10</sup>, G. Soucail<sup>2</sup>, A. Takey<sup>16</sup>, and Ivan Valtchanov<sup>17</sup>

- <sup>1</sup> Institute for Astronomy & Astrophysics, Space Applications & Remote Sensing, National Observatory of Athens, GR-15236 Palaia Penteli, Greece
- <sup>2</sup> IRAP, Université de Toulouse, CNRS, CNES, UT3, Toulouse, France
- <sup>3</sup> AIM, CEA, CNRS, Université Paris-Saclay, Université Paris Diderot, Sorbonne Paris Cité, F-91191 Gif-sur-Yvette, France
- <sup>4</sup> Department of Physics, Aristotle University of Thessaloniki, Thessaloniki 54124, Greece
- <sup>5</sup> Ulugh Beg Astronomical Institute of Uzbekistan Academy of Sciences, 33 Astronomicheskaya str., Tashkent, UZ-100052, Uzbekistan
- <sup>6</sup> Department of Astrophysics, Astronomy & Mechanics, Faculty of Physics, National and Kapodistrian University of Athens, Panepistimiopolis Zografou, 15784, Greece
- <sup>7</sup> Department of Theoretical Physics and Astrophysics, Faculty of Science, Masaryk University, Kotlářská 2, Brno, 611 37, Czech Republic
- <sup>8</sup> Dipartimento di Fisica, Università degli Studi di Torino, via Pietro Giuria 1, I-10125 Torino, Italy
- <sup>9</sup> Argelander-Institut für Astronomie, University of Bonn, Auf dem Hügel 71, D-53121 Bonn, Germany
- <sup>10</sup> Max-Planck-Institut für extraterrestrische Physik, Giessenbachstraße 1, D-85748 Garching, Germany
- <sup>11</sup> LAM, OAMP, Université Aix-Marseille, CNRS, Pôle de l'Étoile, Site de Château Gombert, 38 rue Frédéric Joliot-Curie, 13388, Marseille 13 Cedex, France
- <sup>12</sup> European Space Astronomy Centre, ESA, Villanueva de la Cañada, E-28691 Madrid, Spain
- <sup>13</sup> School of Physics, HH Wills Physics Laboratory, Tyndall Avenue, Bristol, BS8 1TL, UK
- <sup>14</sup> School of Physics & Astronomy, University of Nottingham, University Park, Nottingham, NG7 2RD, UK
- <sup>15</sup> IRFU, CEA, Université Paris-Saclay, F-91191 Gif-sur-Yvette, France
- <sup>16</sup> National Research Institute of Astronomy and Geophysics (NRIAG), 11421 Helwan, Cairo, Egypt
- <sup>17</sup> Telespazio UK for ESA, European Space Astronomy Centre, Operations Department, 28691 Villanueva de la Cañada, Spain

December 14, 2021

## ABSTRACT

**Context.** Cosmological probes based on galaxy clusters rely on cluster number counts and large-scale structure information. X-ray cluster surveys are well suited for this purpose because they are far less affected by projection effects than optical surveys, and cluster properties can be predicted with good accuracy.

**Aims.** The XMM Cluster Archive Super Survey, X-CLASS, is a serendipitous search of X-ray-detected galaxy clusters in 4176 XMM-Newton archival observations until August 2015. All observations are clipped to exposure times of 10 and 20 ks to obtain uniformity, and they span  $\sim 269$  deg<sup>2</sup> across the high-Galactic latitude sky ( $|b| > 20^\circ$ ). The main goal of the survey is the compilation of a well-selected cluster sample suitable for cosmological analyses.

**Methods.** We describe the detection algorithm, the visual inspection, the verification process, and the redshift validation of the cluster sample, as well as the cluster selection function computed by simulations. We also present the various metadata that are released with the catalogue, along with two different count-rate measurements, an automatic one provided by the pipeline, and a more detailed and accurate interactive measurement. Furthermore, we provide the redshifts of 124 clusters obtained with a dedicated multi-object spectroscopic follow-up programme.

**Results.** With this publication, we release the new X-CLASS catalogue of 1646 well-selected X-ray-detected clusters over a wide sky area, along with their selection function. The sample spans a wide redshift range, from the local Universe up to  $z \sim 1.5$ , with 982 spectroscopically confirmed clusters, and over 70 clusters above  $z = 0.8$ . The redshift distribution peaks at  $z \sim 0.1$ , while if we remove the pointed observations it peaks at  $z \sim 0.3$ . Because of its homogeneous selection and thorough verification, the cluster sample can be used for cosmological analyses, but also as a test-bed for the upcoming eROSITA observations and other current and future large-area cluster surveys. It is the first time that such a catalogue is made available to the community via an interactive database which gives access to a wealth of supplementary information, images, and data.

**Key words.** surveys - catalogues - X-rays: galaxies: clusters - galaxies: clusters: general - large-scale structure of Universe - galaxies: groups: general - galaxies: clusters: intracluster medium

## 1. Introduction

Observational cosmology has been coming into increasing focus over the last two decades, propelled by wide-area sur-

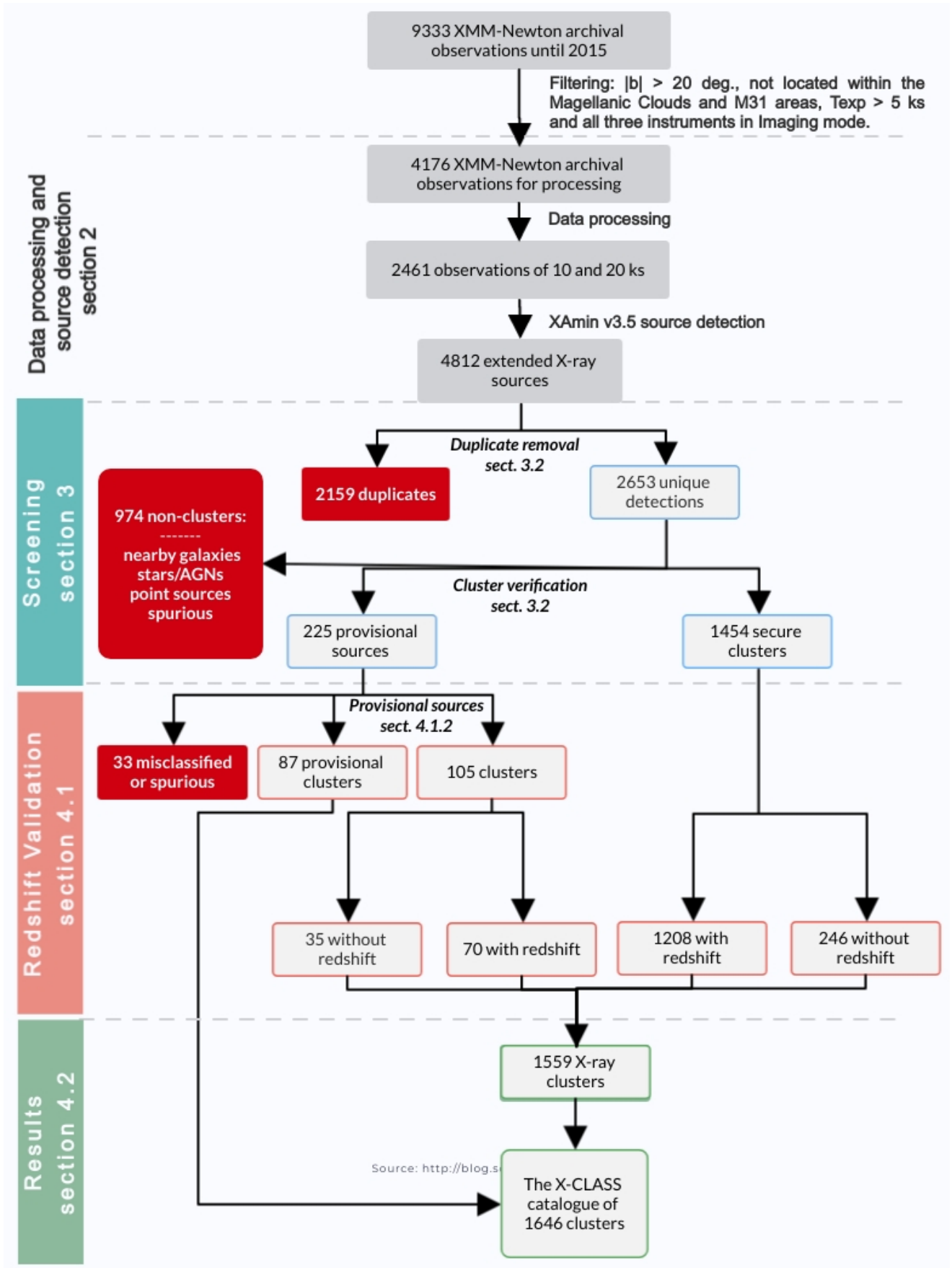


**Fig. 1.** Flowchart of the overall procedure for the compilation of the new X-CLASS cluster catalogue. Red filled frames contain the sources that were discarded.

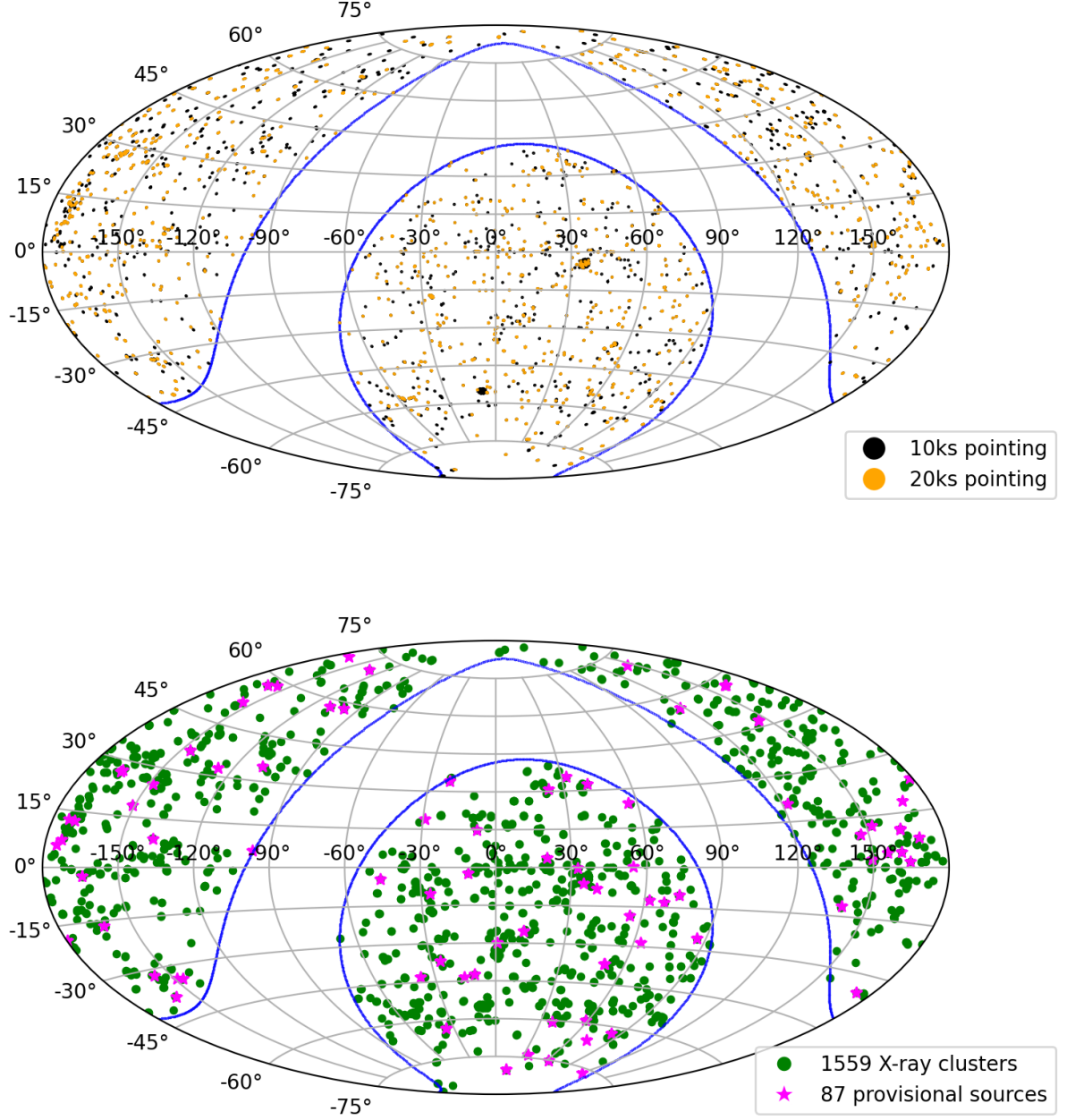


**Fig. 2.** The X-CLASS survey covers a total area of  $269.0 \text{ deg}^2$  by 4176 XMM-Newton archival observations. Top panel: there are 2461 "10 ks" pointings, of which 1309 also have a "20ks" version. This map in equatorial coordinates shows their location on the sky. The blue line marks the limit of  $\pm 20 \text{ deg}$  around the galactic plane. Bottom panel: the 1646 X-ray selected galaxy clusters of the X-CLASS catalogue.

veys, such as for example the *Sloan Digital Sky Survey* (SDSS; Blanton et al. 2017) and the *Wide-field Infrared Survey Explorer* (WISE; Wright et al. 2010), but also by modern observatories like *eROSITA* (Merloni et al. 2012; Predehl et al. 2021) and *Euclid* (Laureijs et al. 2011). All these surveys gain additional value from supplemental multi-wavelength observations, with a growing synergy between space- and ground-based observatories. Wide-area surveys constitute an essential asset for large-scale structure studies because they can provide a unique handle on the abundance of massive objects, a crucial element for cos-

mology. Nevertheless, the collection, analysis, and treatment of the data, in order to create valuable user-friendly catalogues and archives for the scientific community, is increasingly challenging and time-consuming, despite the availability of modern tools and computational capabilities. Therefore, such endeavours are rightfully dubbed 'legacy surveys'.

In this framework, cosmologists seek large samples of galaxy clusters, spanning a wide range of masses and redshifts, in order to use them as cosmological probes. These probes mainly rely on cluster number counts and large-scale structure

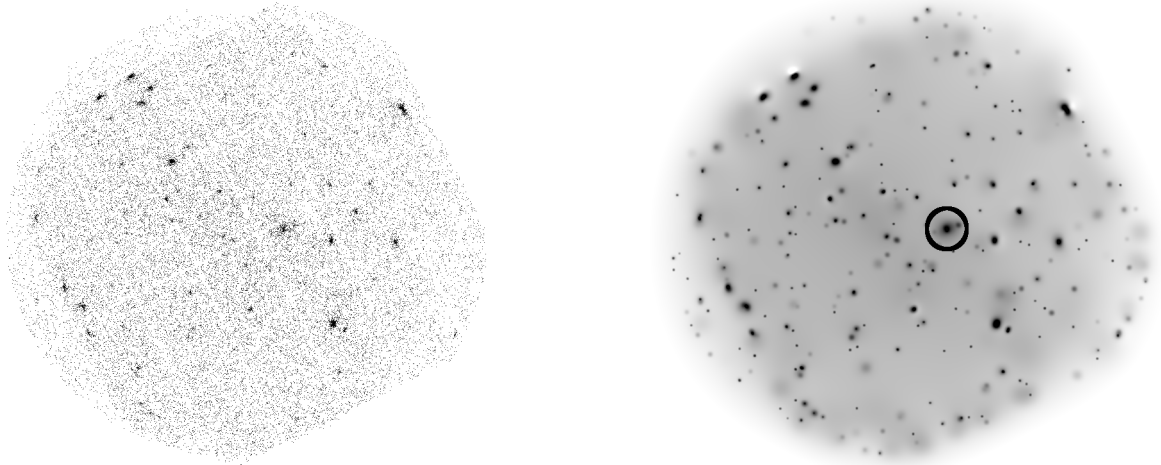


**Fig. 3.** X-ray image in the  $[0.5 - 2]$  keV X-ray band of a 10 ks *XMM-Newton* observation (left panel, mosaic of all three *XMM-Newton* detectors) and the corresponding wavelet filtered image (right panel). The images are not background-subtracted and their diameter is  $26'$ . The circle marks the position of a detected cluster candidate. Similar images are available for all X-CLASS clusters in the public database.

information to capture the evolution of the halo mass function and the halo spatial distribution across cosmic times. Galaxy clusters are the most massive gravitationally bound structures in the Universe. They are mainly dominated by dark matter ( $\sim 85\%$  of the total mass), while the hot X-ray-emitting intracluster medium (ICM) accounts for most of their baryonic mass (e.g. Plionis et al. 2008). Therefore, galaxy clusters can be identified in various wavelengths (e.g. Vikhlinin et al. 2009; Mantz et al. 2010; Rozo et al. 2010; Sehgal et al. 2011; Benson et al. 2013; Planck Collaboration et al. 2014), and X-ray surveys in particular have proven very effective in detecting large numbers of them (e.g. Fassbender et al. 2011; Willis et al. 2013; Pierre et al. 2004, 2016; Takey et al. 2016; Adami et al. 2018) including many at redshifts  $z > 1$ , with the most distant clusters found up to a redshift of  $z \sim 2$  (Santos et al. 2011; Mantz et al. 2018).

The X-ray selection, although possibly biased towards baryon-rich and relaxed clusters (e.g. Andreon et al. 2016; O’Sullivan et al. 2017), presents two main advantages: First, the cluster properties can be self-consistent and easily predicted by *ab initio* models, because the measurable X-ray parameters are closely related to the mass of the cluster (e.g. Frenk et al. 1990; van Haarlem et al. 1997). Second, cluster catalogues are hardly affected by projection effects (e.g. Ramos-Ceja et al. 2019), namely the inclusion of spurious sources resulting from the projection of unrelated systems along the line of sight, because the centrally concentrated X-ray emission clearly indicates the presence of gas trapped in the potential well of a cluster (e.g. Frenk et al. 1990; Reblinsky & Bartelmann 1999).

Consequently, X-ray surveys have had a key role in the systematic search for galaxy clusters, initially with the historical HEAO-1 X-ray observatory (Piccinotti et al. 1982) and then with the Einstein observatory Medium Sensitivity Survey (Gioia et al. 1990; Henry et al. 1992). Many other important surveys have been conducted over the course of the last three decades, starting with the ROSAT observatory, which provided the instrumen-

tation for REFLEX-I, II (Böhringer et al. 2001, 2014), NORAS (Böhringer et al. 2000), MACS (Ebeling et al. 2001), ROSAT-NEP (Henry et al. 2006) and CODEX (Finoguenov et al. 2020; Kirkpatrick et al. 2021), and then by *XMM-Newton* and Chandra observatories, which allowed COSMOS (Scoville et al. 2007; Finoguenov et al. 2007), *XMM-LSS* (Pierre et al. 2007; Clerc et al. 2014), *XMM-BCS* (Šuhada et al. 2012), XCS (Romer et al. 2001; Mehrrens et al. 2012), 2XMMi/SDSS (Takey et al. 2011, 2013, 2014), X-CLASS (Clerc et al. 2012, hereafter CS12), XDCP (Fassbender et al. 2011), and *XMM-XXL* (Pierre et al. 2016; Adami et al. 2018).

In this context, here we present the new X-CLASS catalogue of 1646 X-ray selected clusters followed by a public release. The catalogue is based on all 9333 *XMM* archival observations publicly available until August 2015. All observations were filtered following identical criteria to those in CS12: galactic latitudes above  $20^\circ$  and not located within the Magellanic Clouds and M31 areas, on sky exposure time larger than 5 ks in each of the three European Photon Imaging Camera (EPIC) detectors, and all three instruments in Imaging mode. This led to the selection of 4176 *XMM* pointings that went through an identical processing. In Sect. 2 we present the data processing, the resulting sample of galaxy cluster candidates, and their selection function. In Sect. 3 and 4 we describe the various steps of the screening of the candidates and further analysis of the sample. Finally, in Sect. 5 we describe the public database and in Sect. 6 we discuss the results and compare with other cluster catalogues. The full procedure is also illustrated in Fig. 1 in a flowchart. Throughout this paper, we use  $H_0 = 70 \text{ km s}^{-1} \text{ Mpc}^{-1}$ ,  $\Omega_m = 0.3$ , and  $\Omega_\Lambda = 0.7$ .

## 2. Data processing and source detection

The data processing follows the lines of CS12 with improvements and modifications. We recall here the main steps involved

and highlight the main changes. Basic parameters used during the various data processing steps can be found in Table 1.

The XMM observations were reduced with the latest calibration files available (August 2015) and light curves were created in the high-energy band to monitor the flaring time-intervals. An automated algorithm identified excess variance in the count-rate time histogram in order to determine acceptable count-rate levels which were later included in the GTIs (good time intervals). More specifically, event lists were filtered from proton and solar flares by creating the high-energy event light curves in the [12–14] keV band for MOS and the [10–12] keV band for PN, and flagging out periods of high event rates (rates greater than  $3\sigma$  above the mean observation count rate). Event histograms and the corresponding light curves and cut limits are stored in the online database and are available for all pointings. While the above automated procedure is efficient in removing short periods of high flares, it may fail in observations with a high mean particle background. Therefore, although no systematic human verification is performed at this point, parameters and figures were stored in a database and the overall quality of each observation was subsequently inspected by eye during the screening procedure described in sect. 3.3.

The 4176 observations were homogenised by selecting intervals not contaminated by flares, such that their exposure time in each of the EPIC detectors amounts exactly to 10 ks or 20 ks. This ensures uniformity, enabling the calculation of selection functions. In what follows we refer to XMM observations associated to one of the above two versions as ‘pointings’. Therefore, each original XMM observation may deliver zero, one (10 ks), or two (10 ks and 20 ks) X-CLASS pointings. This resulted in a total of 2461 observations with a 10 ks exposure, of which 1309 also had a 20 ks version. The distribution of these pointings on the sky is shown in Fig. 2. A circular area of radius  $13'$  around each pointing centre defines the geometric area of a pointing on the sky; sources are detected within this off-axis range only, thereby avoiding strongly vignetted areas on the detectors. The total survey geometrical area is computed by means of two-dimensional Monte-Carlo integration, accounting for the overlaps between pointings, and amounts to  $269 \text{ deg}^2$ . We note that pointed observations of clusters have been included in our observation list. Finally, they were processed twice with XAmin v3.5 pipeline (Faccioli et al. 2018) for both exposure times.

Source detection is a three-step process. During the first pass, images in the soft X-ray band, [0.5 – 2] keV, are created and filtered with a wavelet algorithm, as described in Starck & Pierre (1998). According to that paper, this is the best filtering method for X-ray images that contain few photons and Poisson noise. Most importantly, it was demonstrated that this method is very effective in detecting low-flux extended X-ray sources, which is crucial for our short-exposure time survey. An example of such a filtered observation is presented in Fig. 3

During a second step, SExtractor (Bertin & Arnouts 1996) was used for source detection. It provided a centroid estimate, the extent of the X-ray emission, and a rough measurement of brightness. The background level is iteratively estimated in image cells by  $3\sigma$  clipping and a full-resolution background map is constructed by bicubic-spline interpolation. Finally, these parameters served as input for a maximum likelihood fitting routine that applied several source models on the photon image in the soft X-ray band: in particular, a precise point-spread func-

**Table 1.** Data processing parameters

Parameter	value
<b>Event selection:</b>	
MOS event flag selection	#XMMEA_EM
PN event flag selection	(FLAG & 0x2fb002c)==0
MOS patterns	[0:12]
PN patterns	[0:4]
<b>Image:</b>	
Type	Sky
Configuration	Co-addition of EPIC detectors
Pixel size	2.5 arcsec
Filtering	Wavelet transform (8 scales)
<b>SExtractor:</b>	
Background cell side	64 pixel
Background median filtering	4 cells
Detection threshold	$6\sigma$
Detection minimum area	12 pixel
Deblending sub thresholds	64
Deblend min. contrast	0.003

tion (PSF) model and an extended  $\beta$ -model (Cavaliere & Fusco-Femiano 1978) described by

$$S_X(r) \propto \left[ 1 + \left( \frac{r}{EXT} \right)^2 \right]^{-3\beta+1/2},$$

where  $EXT$  is the core radius in arc-seconds and  $\beta = 2/3$ . For either a point-like or an extended source, the MEDIUM PSF model from the XMM calibration data is used. The SExtractor pixel segmentation mask was used to flag out pixels belonging to neighbouring sources included in the box. In contrast to previous XAmin versions, XAmin v3.5 fixed the position of the extended source fit at the value found by SExtractor. This selection yields 4812 extended X-ray sources.

Only sources classified as ‘C1’ in a pointing were used to build the catalogue. These are characterised by a value of their extended-detection likelihood greater than 32, an extent likelihood greater than 33, and an extent (best-fit core-radius) larger than  $5''$  (for more details on these quantities see Faccioli et al. 2018). Simulations of XMM ‘empty’ cosmological fields demonstrated that such thresholds ensure pure samples of extended sources with a controllable selection function (Pacaud et al. 2006). However, XMM-Newton is generally not pointing towards empty fields. The diversity of sources and instrumental artefacts encountered in the archive makes the X-CLASS C1 sample more prone to contamination by non-cluster sources and this is the purpose of the visual inspection process to eliminate those spurious sources (see Sect. 3.3). At this stage, a given C1 detection may appear several times in the source list. This is either due to overlaps between XMM observations, because it appears in both exposure-time versions of the same pointing, or because it has been separated in multiple components, usually by sharp (small-scale) exposure variations due to one (or more) CCD gaps that caused the detection pipeline to segment the detection of extended sources into multiple areas. In the following sections, we describe the cluster selection function and the decontaminating procedure for the removal of duplicate and false detections. We note that clusters detected on observations with

missing detectors were discarded from our list, but can be found in Table B.1.

Owing to the uniform exposure time, simulations allow us to accurately determine the selection function of the X-CLASS cluster sample. However, a large number of extended X-ray detections can be due to various other sources, such as for example nearby galaxies, stars, active galactic nuclei (AGNs), double point-sources, and so on. Most of these sources are not modelled in the simulations and should be discarded before reaching a clean cluster sample. We describe this interactive procedure in the following section.

### 3. Screening of the X-ray cluster candidates

#### 3.1. Previous versions of the catalogue

Our previous analysis of the XMM archive provided a catalogue of 845 sources identified as galaxy clusters among 1514 C1 unique detections on which we performed visual screening. This first catalogue was publicly released in CS12. Sadibekova et al. (2014) cross-matched the redMaPPer optical cluster catalogue (Rykoff et al. 2014) in the northern hemisphere (SDSS photometry) and a subset of the X-CLASS C1 sources. These sources were included as targets of the SPIDERS (*S*pectroscopic *I*dentification of *E*ROSITA *S*ources) follow-up programme (Clerc et al. 2016) in SDSS-IV (Blanton et al. 2017) and are further described in Sect. 4.1.3. In addition, a large follow-up programme with the GROND instrument on the MPG/2.2m telescope at La Silla (Greiner et al. 2008) measured 232 photometric redshifts of X-CLASS clusters using 4-band images and is described in Ridl et al. (2017). All 845 clusters of the first data release are included in the current new X-CLASS catalogue.

#### 3.2. Duplicate removal

The initial list of C1 pipeline-detected sources requires a first-pass inspection in order to remove duplicate entries of single sources. An iterative procedure is performed, coupling automatic and manual associations of multiple detections. Starting from the list of 4812 C1 detections, we grouped sources with a fixed  $10''$  distance criterion, reminiscent of the XMM-Newton PSF extent. We then ensured that the association flags are correctly set, reflecting the nature of the duplicate (e.g. overlapping pointing, secondary exposure, etc.). Only one entry is selected as the main detection according to the following rules: it needs to be detected on the higher exposure pointing (20 ks if present) and in case of conflict, to have the higher value of extent likelihood. This procedure was repeated within  $20''$ ,  $30''$ ,  $40''$ , and  $60''$  correlation radii. Correlations within the larger two radii were supervised and visually validated in order to prevent false associations. During this step, 2159 sources were identified as duplicate detections, leaving 2653 for further visual inspection.

#### 3.3. Cluster verification

Once the duplication check had been applied, all C1 candidates were interactively screened by expert researchers to identify non-clusters, spurious detections, or duplicates missed by the algorithm. To this end, we used overlays of X-ray contours on the Digitized Sky Survey (DSS) images using the dedicated database tool. The purpose of this procedure is twofold: (1) remove nearby galaxies, saturated point-sources, X-ray artefacts, and possible unresolved double-sources that also appear as extended sources, and (2) provide an approximate distance indica-

**Table 2.** Status of the X-CLASS cluster candidates. Sources classified as ‘provisional’ are sources that may not correspond to actual clusters.

status	Dec>0	Dec<0	total
confirmed	556	426	982
tentative	63	31	94
photometric	51	151	202
no status (no $z$ )	109	172	281
provisional (no $z$ )	48	39	87
all	<b>827</b>	<b>819</b>	<b>1646</b>

tor depending on the existence of a conspicuous optical counterpart to the X-ray emission, namely: NEARBY ( $z < 0.3 - 0.4$ ) and DISTANT ( $z > 0.3 - 0.4$ ), where  $z \sim 0.3 - 0.4$  corresponds to the POSS-II plate limit for typical cluster red-sequence galaxies. Other classifications also included ‘nearby galaxy’ and ‘fossil group’. The procedure involved several researchers from the X-CLASS collaboration specialised in cluster science and astronomical observations. Each source was inspected by two or more of the researchers who independently decided on its classification. The final classification, based on these decisions, was then assigned to the sources by two expert moderators, who did not participate in the classification. If the classifications provided by the researchers were discrepant, the decision was arbitrated by the moderators. During this step, 974 detections were discarded. All available redshifts were retrieved for the remaining 1679 cluster candidates using the NED extragalactic database and dedicated follow-up observations.

Out of the 1679 sources, 225 were flagged as ‘provisional’, signifying that the nature of the detected source was dubious, and further investigation was needed. The nature of these sources was thoroughly scrutinised at a later time using deeper optical surveys and more current spectroscopic and photometric data not available during the initial catalogue compilation. Their screening is presented in more detail in Sect. 4.1.2.

## 4. The X-CLASS cluster catalogue

### 4.1. Redshift validation

#### 4.1.1. Visual inspection

Before the compilation of the X-CLASS public catalogue of galaxy clusters, which we present below, we undertook a thorough inspection of all sources considering the availability of wide and recent optical photometric and spectroscopic surveys. We most frequently used DECaLS (Dey et al. 2019), PanSTARRS (Flewelling et al. 2020), and SDSS-DR16 (Blanton et al. 2017), which provided deeper optical images than those of DSS used in our first pass, and a plethora of spectroscopic data. Our procedure included: combined visual inspection of the X-ray and optical images, matching of our candidates with previously released X-ray or optical catalogues of galaxy clusters, collecting all available spectroscopic data to confirm the redshift of the cluster, and producing all relevant meta-data for inclusion in the database.

More specifically, our first action was to search for previously detected galaxy clusters that coincide with our X-ray detection. This information was mostly readily available from our previous matching, but nevertheless we used the NED database for our sources and have included all recent information. All relevant data are stored in the database and are available to the public. When available, the cross-matching provided a first estimation of the cluster redshift. Then, especially in the case where no



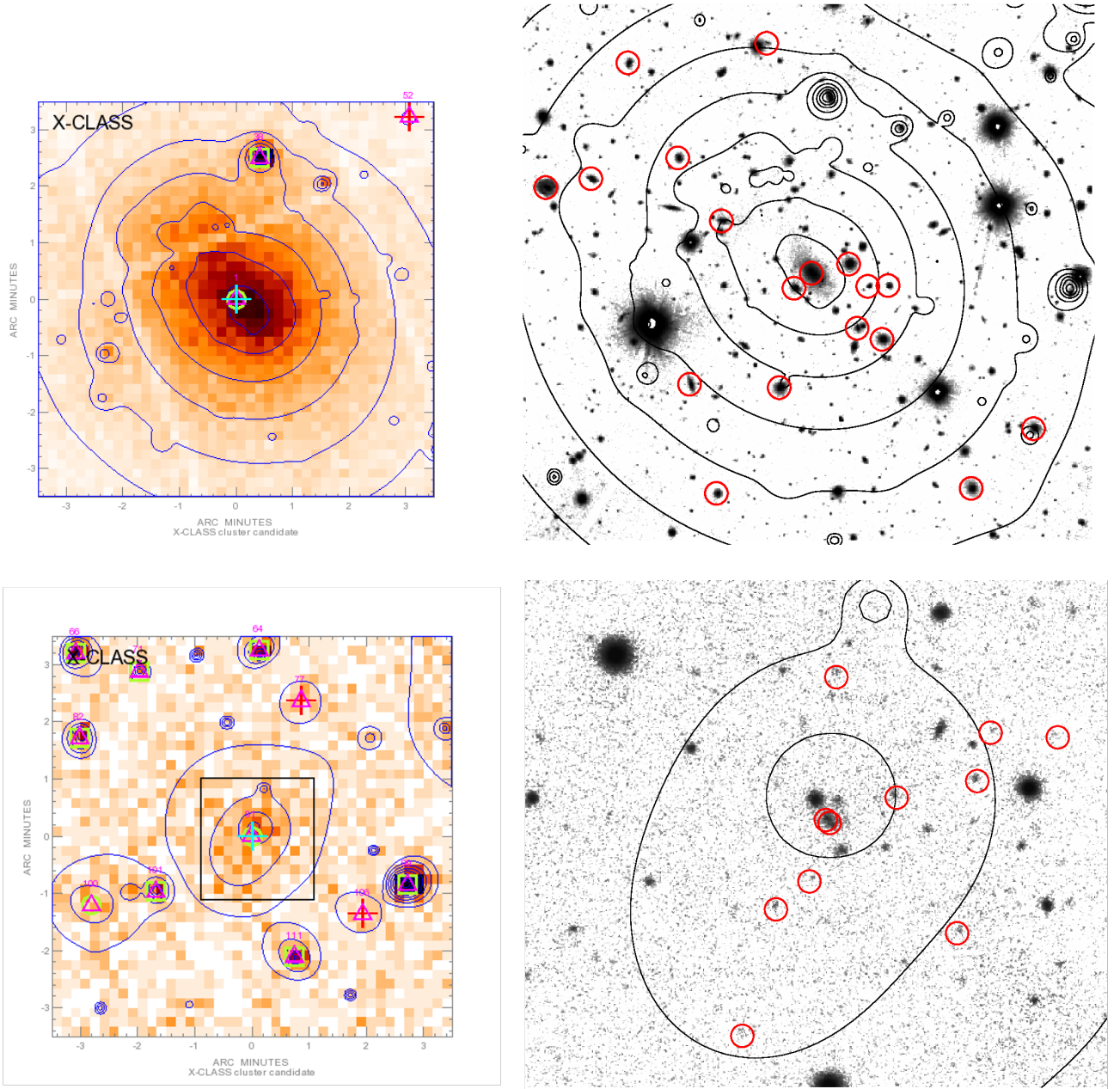


**Fig. 4.** Examples of X-ray-selected galaxy clusters in the X-CLASS survey. Top panels: Cluster Xclass0561 (ABELL 2050) at  $z=0.119$  as confirmed by 19 member galaxies. Bottom panels: Cluster Xclass0219 at  $z=0.791$  as confirmed by 11 member galaxies. Left panels: X-ray images and contours. Green circles (squares) mark detections of extended (point-like) sources as classified by the XAmin pipeline. Straight lines that cross the image are CCD gaps of the XMM-Newton detector. Right panels: i-band optical images from PanSTARRS over-plotted with X-ray contours. Red circles mark the member galaxies with available spectroscopic redshift. In the case of Xclass0561, both X-ray and optical images cover the same sky area, while in the case of Xclass0219 the optical image corresponds to the central region of the X-ray image marked with the black square.

matching cluster was found in the literature, we had to visually inspect the optical and the X-ray image of each cluster candidate. Our first choice for the optical band was PanSTARRS-DR1 colour images (from  $g$  and  $z$  bands) where we found that a concentration of red cluster galaxies is visible up to a redshift of  $z \sim 1$ . PanSTARRS is available for the full northern sky and down to a declination of  $-30$  degrees. For a much more limited sky area, DECaLS survey was also available, which is essential for high-redshift cluster candidates. For the rest of the clusters with no deep optical data, we used the DSS images, as we had previously done during our first pass.

Then, for each cluster with an initial estimation for its redshift, we computed the projected 500 kpc radius. We selected this limiting radius as it roughly corresponds to an average  $R_{500}$  radius for a moderately rich cluster, and we expect to locate the vast majority of cluster galaxies within this range. The same radius was used for the XXL survey cluster sample (Adami et al. 2018). We then collected data from NED and, when available, from SDSS-DR16, because recent spectroscopic data from the latest release were not yet available in NED. To validate the redshift of an X-ray cluster we chose to implement the same

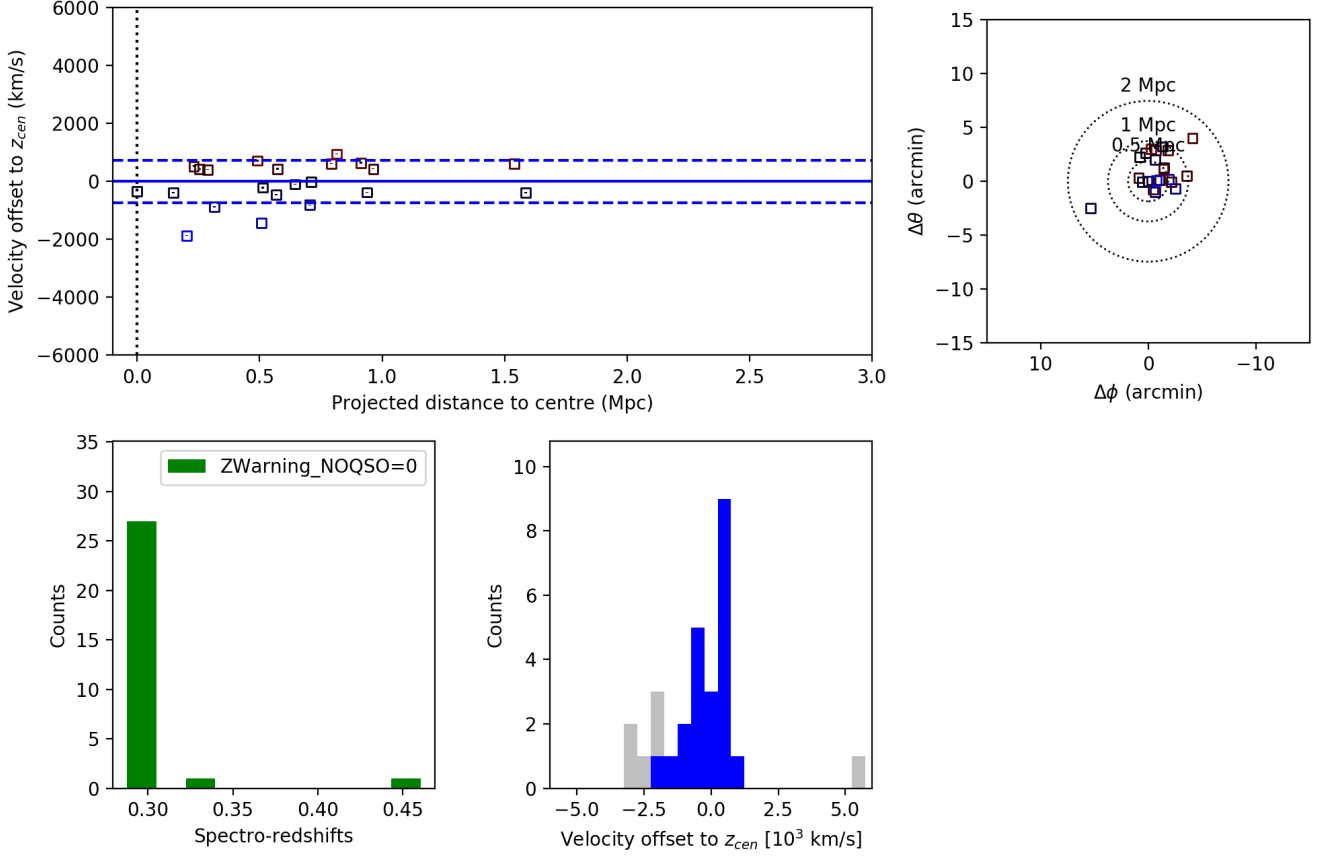


**Fig. 5.** Spectroscopic redshift validation of a cluster using *SPIDERS* follow-up observations, as described in Sect. 4.1.3. The top-left panel shows the distribution of red-sequence galaxies in Xclass0842 as a function of their projected distance to the X-ray centroid and the velocity offset to the mean cluster redshift. Blue dashed lines indicate the standard deviation of the velocity distribution. The top-right panel shows the location of those members projected on the sky, with a similar colour-coding as in the previous panel. The lower-left histogram shows the redshift distribution of galaxies in the red sequence with an associated spectroscopic measurement. The lower-right histogram shows the distribution of members (in blue) and non-members (in grey).

guidelines as for the XXL survey catalogue (Adami et al. 2018). Therefore, the redshift of a cluster can be categorised as follows:

- **Confirmed:** if three or more galaxies with concordant spectroscopic redshifts are found within the 500 kpc radius from the centre of the X-ray detection, or alternatively, if the spectrum of the brightest cluster galaxy (BCG) is available.
- **Tentative:** if one or two galaxies with concordant spectroscopic redshifts are found within the 500 kpc radius.
- **Photometric:** if only photometric redshift information is available in the literature or from our previous dedicated follow-up (Ridl et al. 2017).
- **Provisional:** for cases where the available information does not allow us to verify the existence of a galaxy cluster in this position. Further follow-up observations are needed to safely classify these sources. Although these sources are part of the X-CLASS catalogue, they are not included in the on-line database, but can be found in Appendix D.

All cluster candidates were reviewed by at least two researchers. However, visual inspection and redshift confirmation was especially critical for the 225 sources previously classified as ‘provisional’, for which we followed the more thorough procedure described in the following section.

#### 4.1.2. Provisional sources

As provisional cases were more challenging for the reviewers, each source was further inspected by two more consortium members. Their task was to simply classify the detection as a true or false cluster, considering all available optical and X-ray data. Out of the 225 sources, 70 were already validated as true clusters (49 confirmed, 12 tentative, and 9 photometric) and were used to test the reliability of the reviewers. For this step, we considered the classifications of seven researchers (different from those of the previous section), while we discarded those of the two researchers that gave the greatest number of false answers with respect to the already validated sources.

Finally, we require full agreement between the researchers in order to characterise a source as a true cluster, or a spurious or misclassified detection, while sources with discrepant classifications kept their ‘provisional’ status. More precisely, 33 provisional sources were classified as ‘inexistent’ and were discarded from the catalogue, while 35 were identified as true clusters and entered the catalogue without any redshift information. The remaining 87 sources retained the ‘provisional’ status, and, though kept in the main public catalogue, are not published online, but are included in Appendix D of the present paper for the interested reader, especially as this list may contain high-redshift cluster candidates.



Misclassified detections are usually due to a point-like source embedded in the extended X-ray emission of a nearby cluster, while high background may also play an important role. The majority of the spurious or misclassified cluster candidates have no visually detected counterpart in the optical band; their X-ray emission was limited within less than  $10''$  radius and was usually centred on an optical point source. In addition, we applied machine-learning classification to our provisional sources in order to test the efficiency of such methods in difficult cases. The results are presented in Appendix A.

#### 4.1.3. Spectroscopic follow-up with SPIDERS

A subsample of the previous X-CLASS sample was selected for spectroscopic follow-up within the frame of SPIDERS (SPectroscopic IDentification of *eROSITA* Sources), a dedicated survey for a homogeneous and complete sample of X-ray active galactic nuclei and galaxy clusters over a large fraction of the sky (Clerc et al. 2016; Dwelly et al. 2017; Salvato et al. 2018; Comparat et al. 2020). The (BOSS) spectrograph mounted on the SDSS-2.5m telescope at Apache Point Observatory (Gunn et al. 2006) was used. The sample was compiled based on the correlation of X-ray sources from X-CLASS with the RedMapper optical cluster catalogue, as described in Sadibekova et al. (2014) and Clerc et al. (2016). The current catalogue contains 124 validated clusters (out of the 142 targeted) with SPIDERS follow-up spectroscopy up to a redshift of  $z \sim 0.6$ . The program led to the collection of 1134 spectra in X-CLASS red sequences, with a redshift success rate approaching 99% (Clerc et al. 2020). The median number of galaxies with concordant redshifts used for the redshift validation was ten. Membership is assigned with an algorithm iteratively performing  $3\sigma$  clipping around the mean redshift. Manual refinements are then allowed in the case of degenerate situations or failures due to the low number of spectroscopic redshifts available. An example cluster is shown in Fig. 5 (see also Kirkpatrick et al. 2021). The list of clusters confirmed with SPIDERS spectroscopy can be found in Table C.1 of the Appendix.

#### 4.2. The new X-CLASS catalogue

Following the above classification scheme, the catalogue comprises 1278 X-ray-selected clusters with redshift information: 982 spectroscopically confirmed clusters, 94 with a tentative redshift, and 202 with a photometric redshift. These three categories represent  $\sim 78\%$  of the total cluster catalogue and their redshift distribution is presented in Fig. 6. The final catalogue includes an additional 281 clusters with no redshift information. The results are summarised in Table 2 where they are also split between the two hemispheres, because the availability of observational data is very different. This leads to less confirmed clusters and more with no redshift information in the southern hemisphere.

In addition to the above sources, a small number of detections were flagged as ‘inexistent’ ( $\sim 2\%$ ) and were removed from the catalogue, while the 87 sources that were classified as ‘provisional’ can be found in Table D.1 of the current paper. We caution the interested reader that this list may include a number of spurious or misclassified sources.

Coordinates and redshifts of all cluster galaxies are stored in the cluster database. In the case of confirmed clusters, a histogram with all available spectroscopic redshifts within the corresponding search radius was also produced using the online tool in NED.

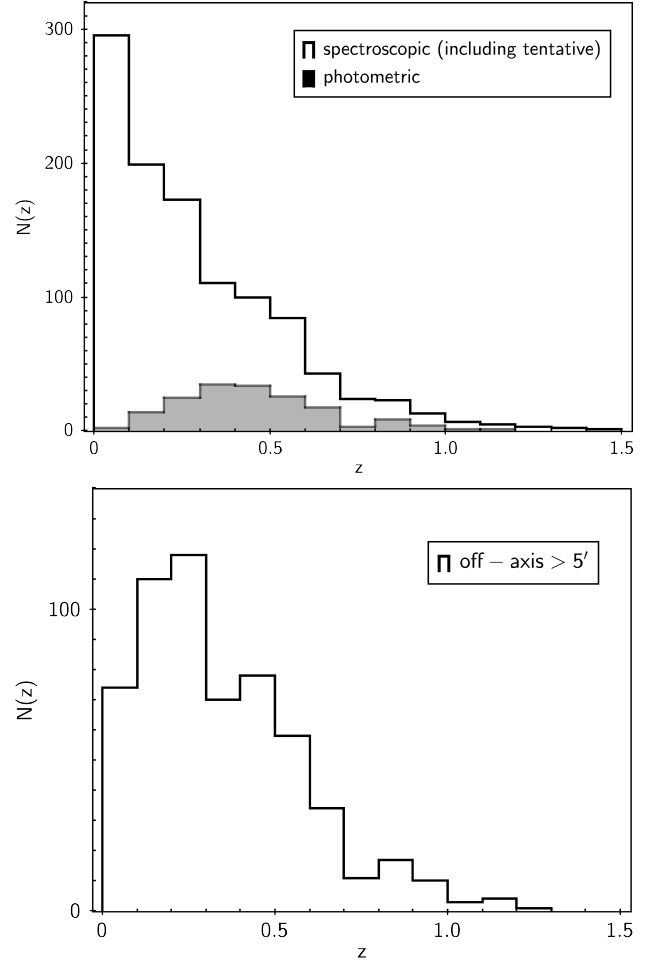


**Fig. 6.** Top panel: Redshift distribution of the X-CLASS clusters with available spectroscopic or photometric redshift. Bottom panel: Redshift distribution for clusters found outside the central  $5'$  of the XMM pointings, which excludes pointed observations that bias our sample towards low-redshift values. This distribution peaks around  $z_{med} = 0.29$ .

#### 4.3. X-ray count-rate measurements

In the database we provide two different X-ray count-rate measurements: the pipeline quantities and a more accurate measurement using a count-rate curve of growth method developed by our team (Clerc et al. 2012).

The pipeline value is the total background-subtracted source count rate in the three XMM-Newton detectors (MOS1+MOS2+PN) in the  $[0.5 - 2]$  keV band. This is an automatic measurement provided by the XAmin pipeline fitting procedure (raw pipeline output). It is a measure of the total count rate integrated out to infinity under the assumption that the best-fitting model is correct. The background is locally defined within a box around each source as a flat component that includes both the photon (vignetted) and the particle background, and is fitted simultaneously with the source model parameters. This is a simplified approach because the particle background is in general not flat across the EPIC detectors. Nevertheless, it is justified by the small extent of the vast majority of our sources.

In addition, all sources detected with the XAmin pipeline were subjected to a semi-interactive procedure, described in sect. 2.4 of CS12, in order to provide more accurate X-ray flux measurements. The sources were assumed to have a circular symme-

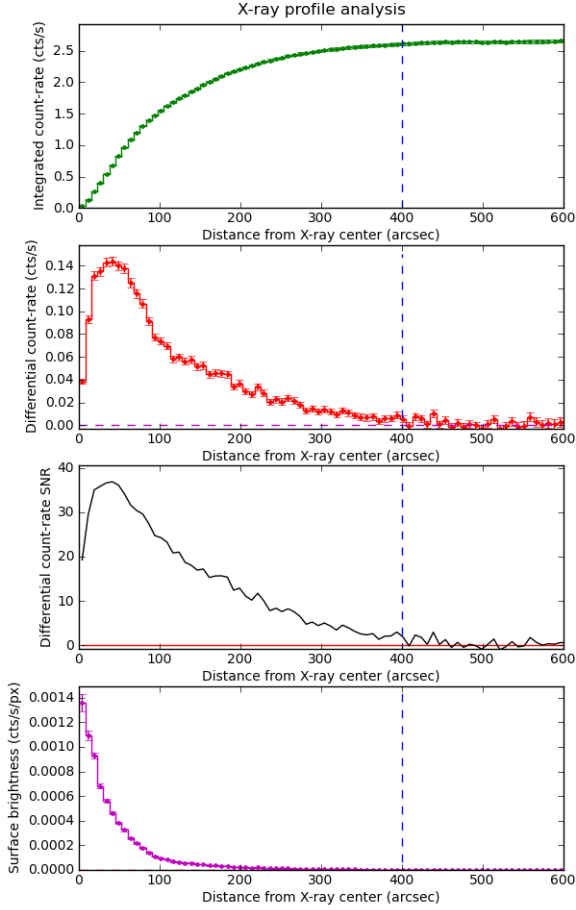


**Fig. 7.** Interactive background-subtracted count-rate measurement of the X-ray cluster Xclass0047, as described in Sect 4.2. The blue dashed line in each of the panels indicates the manually defined radius, within which the count-rate measurement is performed.

try to extrapolate measurements on missing parts (masks, CCD gaps, and borders) of the detectors, and to integrate the count rate in concentric annuli. The possibility to interactively alter the segmentation masks was open to the users. The count rate (cts/s) is the mean number of cluster X-ray photons collected by the three detectors in the direction of the optical axis in one second. The total count rate is the sum of all detector count-rate measurements. A count-rate growth curve as a function of cluster radius is computed from the total count rate. The background was modelled similarly to the respective XAmin automatic procedure. The flat and vignettted background levels were fitted on data extracted in a circular annulus around the source of interest, whose width and position are manually adjusted.

The procedure consists of two steps. The first is an interactive (manual) mode enabling the user to: (a) refine the X-ray cluster centre, (b) remove or correct areas incorrectly masked by XAmin (CCD gaps, unresolved blended sources, FOV edge cases), (c) re-estimate the background level according to the cluster brightness and extension to get a more precise count-rate measurement, (d) optimise the measurements in cases where the source is detected on the missing part of MOS1, and (e) set a more accurate and reliable value for the source radii  $R_{fit}$  when the growth curve algorithm has failed because of background overestimation (field source contamination, missing part

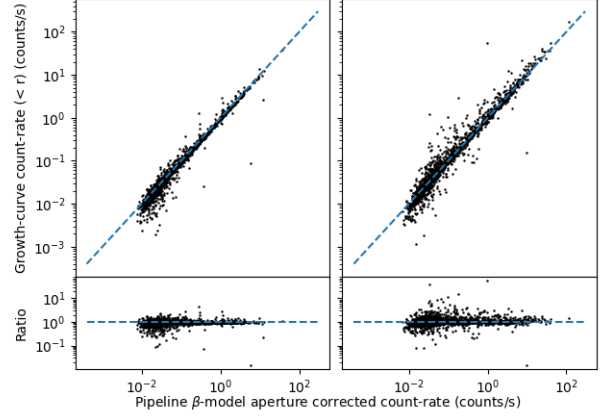


**Fig. 8.** Comparison between the count rate measured by the source detection pipeline and the manual curve of growth analysis for the 1559 galaxy clusters in the sample. The values represent the equivalent on-axis count rate in the [0.5–2] keV energy band combining all three detectors, estimated within identical apertures  $r$ . In the left panel,  $r = 1$  arcmin. In the right panel  $r = R_{fit}$ , a radius that is unique to each source and adapted to the signal-to-noise ratio in the measurement images. In both panels, the dashed line represents equality. Uncertainties are only available for manual measurements and are not shown in this figure.

of MOS1, edge effects). In usual conditions,  $R_{fit}$  corresponds to the annulus in which the cluster count-rate uncertainty is compatible with background fluctuations.

The second step is automatically executed when the cluster parameters in the interactive mode have been set. During this step, the count rates are computed in six different bands, namely [0.5 – 2], [2 – 10], [0.5 – 0.9], [1.3 – 2], [2 – 5] and [5 – 7] keV, using a full exposure to obtain the highest signal-to-noise ratio. Settings and measurements for each cluster separately are available in the X-CLASS database on their *profile* page. An example of the above procedure is illustrated in Fig. 7.

A comparison between the two kinds of count-rate measurements is shown in Fig. 8 for 1559 clusters for which both measurements are available. For the purpose of this comparison, the count-rate growth curve of each source is evaluated at a fixed angular aperture radius  $r = 60''$  and at the source radius  $r = R_{fit}$ . On the other hand, the pipeline count-rate measurement is aperture-corrected by means of the best-fit surface brightness model. For sources brighter than  $0.1 \text{ counts s}^{-1}$  the agreement between the two measurements is very good: within arcminute-sized apertures, the manually measured count rate is 6% lower on average than the pipeline count rate; it is 4% higher within  $R_{fit}$ . At lower count rates, manual measurements enable a more accurate centre positioning, refined background estimates, and more comprehensive source masking, hence recovering most of the failures due to automated model fitting.

#### 4.4. Cluster selection function

In order to model the X-ray-extended selection function of the X-CLASS catalogue, we produced XMM simulations enriched with additional beta-models of a smaller extent, but otherwise identical to those used in CS12. These simulations faithfully reproduce the characteristics of the detectors. We added AGNs following a published  $\log N$ – $\log S$  relation (Marconi & Hunt 2003),

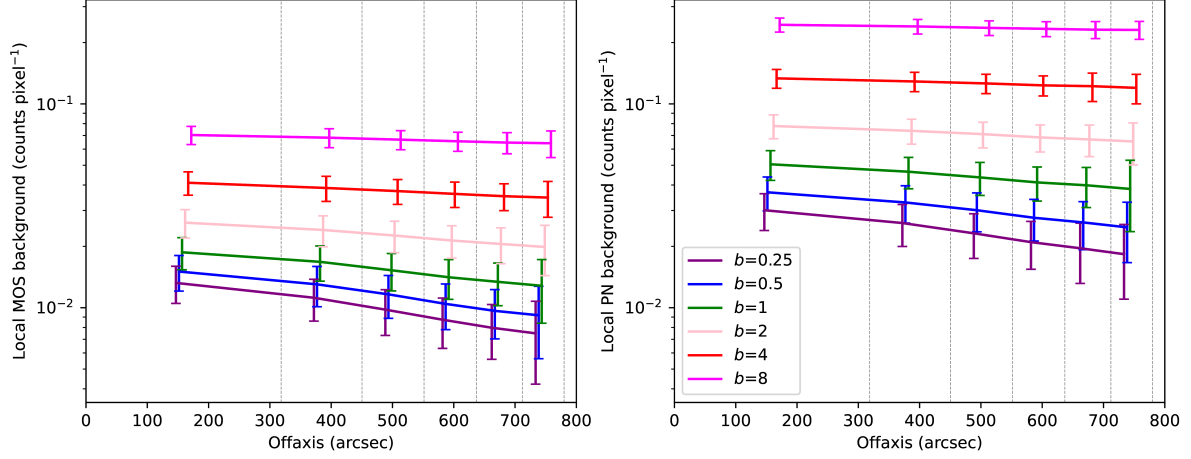


**Fig. 9.** Calibration of the particle background  $b$  parameter as a function of the local background fit by XAmin 3.5 in various equal-area off-axis bins for MOS (left) and PN (right panel) based on the point-source simulations. Off-axis bin boundaries are represented with vertical dashed lines and data points are slightly shifted on the x-axis for readability. Here,  $b = 1$  is the so-called nominal particle background, i.e. close to the most common level encountered in X-CLASS observations. In simulations, particle background is injected at a level of  $b$  times the nominal value. The pixel size is  $2.5'' \times 2.5''$ .

and unresolved AGNs modelled as a vignettted background component. Unvignettted particle background was also added, parameterised with a factor  $b$ . This factor represents the level of enhancement compared to the nominal background level,  $b=1$ . Simulations are performed with values of  $b=0.25, 0.5, 1, 2, 4$ , and  $8$ , and the values of the added particle background as a function of off-axis distance are presented in Fig. 9. Optionally, extended sources as beta-models are distributed at random places on the detector. Their total count rate (in 0.5–2 keV) and apparent core radius are varied while beta is held fixed at  $2/3$ . The range of count rates spans (0.0025 counts/s – 0.5 counts/s). The range of core radii is (3, 5, 10, 20, 50, 100) arcsec.

The number of simulations amounts to 540 for each value of  $b$  and for exposure times of 10 and 20 ks. These were all processed with XAmin v3.5 as was briefly described in Sect. 2.1 to exactly mimic observations. We use a  $37.5''$  matching radius for clusters, independently of their extent, flux, and so on, for consistency with previous works (e.g. Pacaud et al. 2006). Sources with multiple associations are ascribed to their nearest neighbour.

In Fig. 10 we present the detection probability of sources within  $13'$  off-axis radius from the centre of the observation, for an exposure time of  $T_{\text{exp}}=10$  ks and for background level  $b=1$ . It is apparent that the X-CLASS catalogue is not a flux-limited sample, but the selection is rather two-dimensional depending on the extent of the source. Figure 11 illustrates the impact of increasing the background level or the exposure time on the selection of typical X-CLASS clusters (core radii around 20 arcsec). A twofold increase in exposure time provides more numerous low-flux clusters as long as the particle background level remains below three times the fiducial value  $b = 1$ .

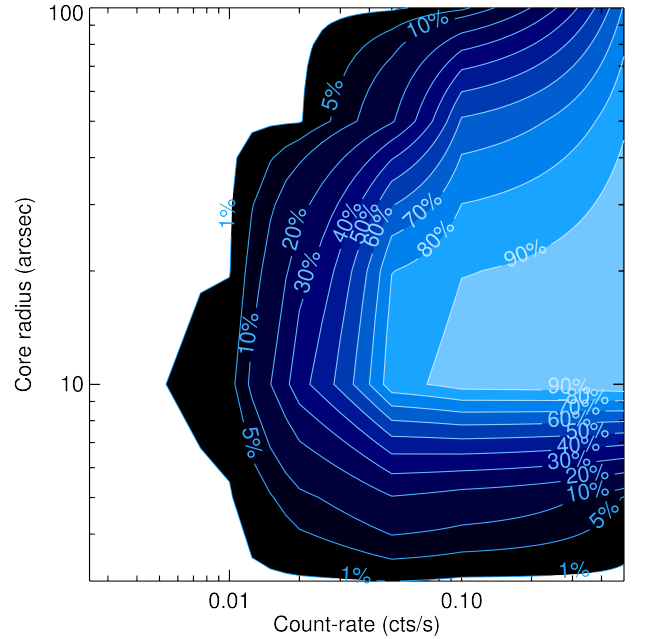


**Fig. 10.** Contours of the C1 detection probability as a function of total count rate [0.5 – 2] keV and input core radius of the beta model. Exposure time of  $T_{\text{exp}}=10$  ks and background value of  $b = 1$  were used.

**Table 3.** X-CLASS cluster database view.

(1) X-CLASS unique ID number and link to images and pipeline outputs, (2) right ascension (pipeline automatic measurement), (3) declination (pipeline automatic measurement), (4) right ascension (interactive refined measurement\*), (3) declination (interactive refined measurement\*), (6) link to NED data, (7) observation ID and link to the observation and data processing information page, (8) link to the redshift information page, (9) redshift status, (10) total X-ray count-rate in the [0.5–2 keV] band (pipeline output), (11) link to the interactive X-ray count-rate measurement page.

\*for more details see sect. 4.2

Xclass (1)	RA pipeline (deg.) (2)	Dec pipeline (deg.) (3)	RA measured (deg.) (4)	Dec measured (deg.) (5)	NED (6)	Obs (7)	redshift (8)	status (9)	total rate (counts/sec) (10)	profile (11)
<a href="#">0020</a>	193.4380	10.1954	193.4380	10.1951	<a href="#">go</a>	<a href="#">0001930301_10ks</a>	<a href="#">0.654</a>	confirmed	0.049	<a href="#">data</a>
<a href="#">0023</a>	194.2860	-17.4119	194.2920	-17.4064	<a href="#">go</a>	<a href="#">0010420201_10ks</a>	<a href="#">0.047</a>	confirmed	3.738	<a href="#">data</a>
<a href="#">0033</a>	193.6790	-29.2227	193.6740	-29.2230	<a href="#">go</a>	<a href="#">0030140101_10ks</a>	<a href="#">0.056</a>	confirmed	5.882	<a href="#">data</a>
<a href="#">0034</a>	193.5950	-29.0162	193.5930	-29.0131	<a href="#">go</a>	<a href="#">0030140101_10ks</a>	<a href="#">0.053</a>	confirmed	4.362	<a href="#">data</a>
<a href="#">0035</a>	196.2740	-10.2802	196.2740	-10.2787	<a href="#">go</a>	<a href="#">0032141201_10ks</a>	<a href="#">0.34</a>	photometric	0.047	<a href="#">data</a>
<a href="#">0038</a>	36.5674	-2.6651	36.5677	-2.6663	<a href="#">go</a>	<a href="#">0037981801_10ks</a>	<a href="#">0.056</a>	confirmed	0.167	<a href="#">data</a>
<a href="#">0039</a>	36.4987	-2.8272	36.4990	-2.8275	<a href="#">go</a>	<a href="#">0037981801_10ks</a>	<a href="#">0.281</a>	confirmed	0.033	<a href="#">data</a>
<a href="#">0040</a>	35.1871	-3.4339	35.1886	-3.4339	<a href="#">go</a>	<a href="#">0037982601_10ks</a>	<a href="#">0.327</a>	confirmed	0.050	<a href="#">data</a>
<a href="#">0042</a>	150.1230	-19.6282	150.1220	-19.6292	<a href="#">go</a>	<a href="#">0041180301_10ks</a>		no redshift	0.057	<a href="#">data</a>
<a href="#">0044</a>	202.4460	11.6835	202.4490	11.6848	<a href="#">go</a>	<a href="#">0041180801_10ks</a>	<a href="#">0.204</a>	confirmed	0.087	<a href="#">data</a>
<a href="#">0047</a>	172.9830	-19.9229	172.9800	-19.9271	<a href="#">go</a>	<a href="#">0042341001_10ks</a>	<a href="#">0.307</a>	confirmed	3.254	<a href="#">data</a>
<a href="#">0048</a>	173.0280	-19.8611	173.0280	-19.8614	<a href="#">go</a>	<a href="#">0042341001_10ks</a>	<a href="#">0.307</a>	confirmed	0.154	<a href="#">data</a>
<a href="#">0050</a>	172.8110	-19.9326	172.8130	-19.9343	<a href="#">go</a>	<a href="#">0042341001_10ks</a>	<a href="#">0.46</a>	photometric	0.025	<a href="#">data</a>
<a href="#">0051</a>	177.6130	1.7580	177.6160	1.7580	<a href="#">go</a>	<a href="#">0044740201_10ks</a>		no redshift	0.036	<a href="#">data</a>
<a href="#">0054</a>	145.9370	16.7402	145.9380	16.7381	<a href="#">go</a>	<a href="#">0046940401_10ks</a>	<a href="#">0.18</a>	confirmed	0.136	<a href="#">data</a>
<a href="#">0056</a>	145.8820	16.6656	145.8860	16.6671	<a href="#">go</a>	<a href="#">0046940401_10ks</a>	<a href="#">0.255</a>	confirmed	0.202	<a href="#">data</a>
<a href="#">0057</a>	145.9920	16.6871	145.9950	16.6875	<a href="#">go</a>	<a href="#">0046940401_10ks</a>	<a href="#">0.253</a>	confirmed	0.057	<a href="#">data</a>
<a href="#">0059</a>	31.9565	2.1553	31.9576	2.1567	<a href="#">go</a>	<a href="#">0052140301_20ks</a>	<a href="#">0.334</a>	photometric	0.042	<a href="#">data</a>
<a href="#">0062</a>	44.1414	0.1037	44.1417	0.1033	<a href="#">go</a>	<a href="#">0056020301_10ks</a>	<a href="#">0.362</a>	confirmed	0.778	<a href="#">data</a>
<a href="#">0065</a>	339.2510	-15.2730	339.2520	-15.2731	<a href="#">go</a>	<a href="#">0056021601_10ks</a>	<a href="#">0.31</a>	photometric	0.316	<a href="#">data</a>
<a href="#">0075</a>	10.4501	-9.4575	10.4507	-9.4569	<a href="#">go</a>	<a href="#">0723802201_20ks</a>	<a href="#">0.056</a>	confirmed	15.529	<a href="#">data</a>
<a href="#">0078</a>	10.7223	-9.5697	10.7225	-9.5701	<a href="#">go</a>	<a href="#">0065140201_10ks</a>	<a href="#">0.41</a>	photometric	0.101	<a href="#">data</a>
<a href="#">0079</a>	10.5228	-9.6026	10.5231	-9.6029	<a href="#">go</a>	<a href="#">0065140201_10ks</a>	<a href="#">0.055</a>	tentative	0.033	<a href="#">data</a>
<a href="#">0082</a>	39.4926	-52.3934	39.4929	-52.3937	<a href="#">go</a>	<a href="#">0067190101_10ks</a>	<a href="#">0.136</a>	confirmed	0.259	<a href="#">data</a>
<a href="#">0083</a>	148.424	1.6999	148.424	1.6995	<a href="#">go</a>	<a href="#">0070940401_10ks</a>	<a href="#">0.097</a>	confirmed	0.796	<a href="#">data</a>
<a href="#">0086</a>	348.765	-58.9351	348.766	-58.9354	<a href="#">go</a>	<a href="#">0081340301_10ks</a>	<a href="#">0.44</a>	photometric	0.034	<a href="#">data</a>
<a href="#">0087</a>	349.094	-59.0752	349.095	-59.0756	<a href="#">go</a>	<a href="#">0081340301_10ks</a>	<a href="#">0.62</a>	photometric	0.036	<a href="#">data</a>
<a href="#">0088</a>	183.394	2.8953	183.395	2.8963	<a href="#">go</a>	<a href="#">0081340801_10ks</a>	<a href="#">0.410</a>	confirmed	0.190	<a href="#">data</a>
<a href="#">0095</a>	190.102	-11.8008	190.103	-11.8011	<a href="#">go</a>	<a href="#">0084030101_10ks</a>	<a href="#">0.19</a>	photometric	0.078	<a href="#">data</a>
<a href="#">0096</a>	9.2778	9.1566	9.2765	9.1583	<a href="#">go</a>	<a href="#">0084230201_20ks</a>	<a href="#">0.252</a>	confirmed	2.441	<a href="#">data</a>

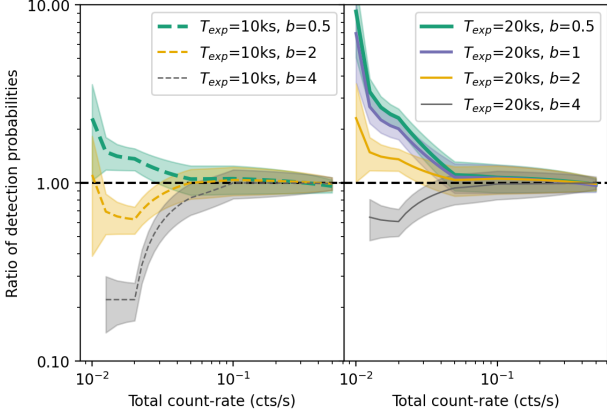


**Fig. 11.** Variation of the C1 detection efficiency with exposure time and background level. Curves show the ratio relative to the probability shown in Fig. 10 (exposure time of 10 ks and  $b = 1$ ), assuming an apparent core radius  $R_c = 20''$ . Shaded regions represent the standard deviation around these values, which depends on the number of simulated clusters. Only points with more than nine detected simulated clusters are shown.

## 5. The X-CLASS database

The X-CLASS database is built using the MySQL database management system and is accessible to a user through a Java Web Application. The database contains all catalogue meta-data, images and plots, which are available in PNG format generated from pipeline output. The cluster table is dynamically generated using a selection interface and is then displayed as an HTML web page. Several criteria (redshift, X-CLASS name, x-ray parameters, sky area, etc.) can be applied to refine (constrain) the cluster selection. For each cluster position, there are pre-configured requests to the external astronomical data servers (CDS, NED, NASA/IPAC IRSA) enabled to display optical counterparts and overlays within 3 *arcmin*. A user manual along with relevant documentation is also available online, as well as the list of X-CLASS publications. The database is hosted in CC-IN2P3 (Centre de Calcul de l'IN2P3 at Lyon in France) and is publicly available online in <https://xmm-xclass.in2p3.fr/>.

### 5.1. Cluster table

The first 20 entries are listed in Table 3, sorted according to increasing RA, while the full version of the catalogue table can be retrieved from the Vizier server at the CDS ([link will be added](#)). From the database graphical interface, the catalogue table provides the following fields for each cluster:

1. *Xclass* – a unique cluster identifier.
2. *RA* – pipeline-measured right ascension.
3. *Dec* – pipeline-measured declination.
4. *Obs* – XMM pointing where the cluster is detected.
5. *NED* – the NED search is within 3 *arcmin*, the page is automatically generated using the AladinLite webapp.
6. *redshift* – cluster redshift, linked to the redshift validation page.
7. *status* – redshift validation status (e.g. photometric, spectroscopic).
8. *total rate* – pipeline total count rate.
9. *profile* – more accurate count-rate quantities from *FluxMes* measurements for six X-ray bands within  $R_{fit}$

## 6. Discussion and comparison with other catalogues

On one hand, the homogeneous selection of the X-CLASS clusters on homogenised observations of 10 and 20 ks exposures simplifies the computation of their selection function and their use in cosmology studies. On the other hand, because of the above selection, the comparison with other similar datasets is difficult (see also relevant discussion in CS12). Nevertheless, within 1' we cross-correlated the X-CLASS catalogue with other X-ray-selected cluster catalogues in order to examine the redshift agreement of the common sources. In Fig. 12 we present such a comparison with two catalogues of X-ray-detected clusters by XMM-Newton, XCS (Mehrtens et al. 2012), and 2XMMi/SDSS (Takey et al. 2014), and two by ROSAT, MCXC (Piffaretti et al. 2011) and CODEX (Finoguenov et al. 2020). There is good agreement between redshifts, especially with the MCXC catalogue. We note that in many cases redshifts were obtained from the same source. In cases of large discrepancies we examined our cluster identifications and redshift validation. In most of the discrepant cases, our more recent and updated data allow for a more accurate redshift estimation, while in a limited number of cases, the matched X-ray detections are correlated with different optical counterparts.

We also examined the X-ray luminosity distribution of the matched X-CLASS/XCS cluster sample in order to identify any systematic bias in our selection. In Fig. 13 we plot the distribution of  $L_{500}[0.05 - 100]$  keV, as estimated in Mehrtens et al. (2012) within the  $R_{500}$  radius, for both the matched and the full XCS sample. The two samples have very similar luminosity distributions, as also confirmed by a two-sample Kolmogorov-Smirnov test. Therefore, the matched sample is an unbiased subsample of the total XCS sample.

In addition we cross-correlated our catalogue with the 4XMM-DR10 catalogue (Webb et al. 2020). This catalogue includes a large number of extended X-ray sources and their fitting parameters, but does not include any redshift estimation or further examination of their nature. The large majority of the X-CLASS sources are correlated to an extended source in the 4XMM catalogue within 1' radius. However, 191 sources are absent, most of which have a provisional status or no redshift information, and inspection of their optical counterpart places them at high redshift. In addition, they usually have a low value for the extent likelihood parameter, as computed by the XAmin pipeline. Nevertheless, a high fraction ( $\sim 27\%$ ) of the uncorrelated clusters have a 'confirmed' or 'photometric' status, usually below  $z = 0.6$ .

## 7. Summary

We present the detection pipeline, selection function, visual inspection, screening, and redshift confirmation of a large number of X-ray-detected galaxy clusters in 4176 archived *XMM-Newton* images. The total number reaches 1646 clusters over 269  $\text{deg}^2$  and the catalogue is publicly accessible via an interactive database constructed and maintained by the X-CLASS collaboration. The database not only allows the selection of a cluster subsample based on a large variety of criteria, but also gives access to a wealth of meta-data, images, plots, and supplementary information.

The homogeneous selection of the cluster samples over 10 and 20 ks exposures allows the use of the X-CLASS catalogue for cosmological analyses, provided the impact of pointed clusters is accounted for. In addition, the large sky area makes it



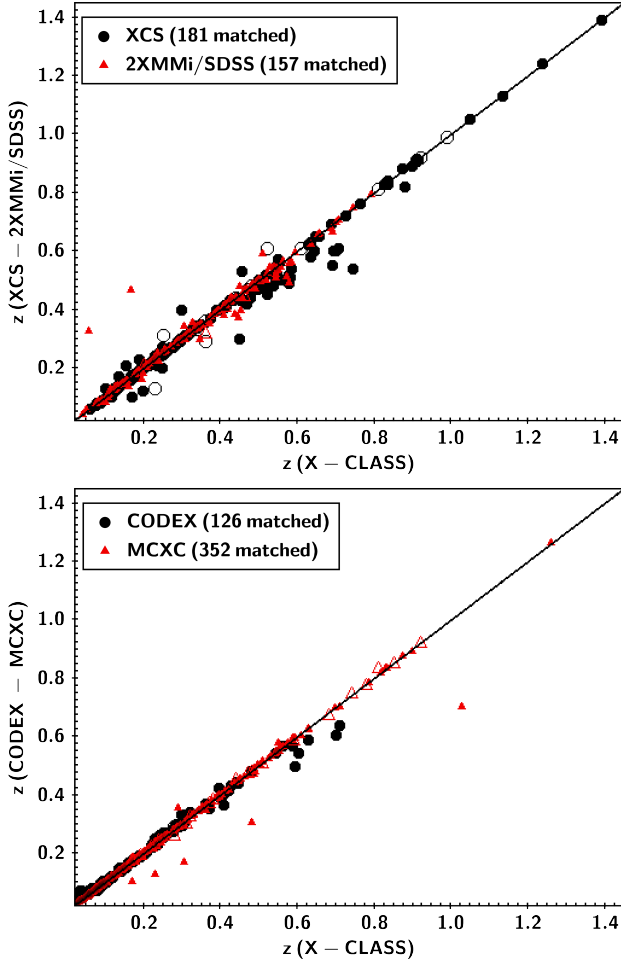


**Fig. 12.** Redshift comparison between the X-CLASS catalogue and various other X-ray-selected cluster samples. All catalogues include both clusters with spectroscopic and photometric redshifts, except for CODEX, which includes only photometric redshift. The filled (open) shapes mark clusters with spectroscopic (photometric) redshift.

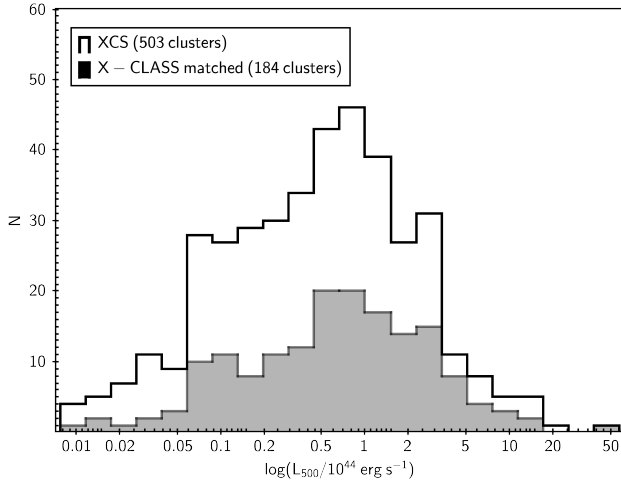


**Fig. 13.** X-ray bolometric luminosity  $L_{500}[0.05 - 100]$  keV distribution of the matched X-CLASS and XCS cluster catalogues. According to a KS two-sample test the null hypothesis that the two samples originate from the same parent distribution cannot be rejected.

suitable as a test bed for current and future large-area cluster surveys, such as the ones that will be carried out by the *eROSITA* (Merloni et al. 2012; Predehl et al. 2021), *Athena* (Nandra et al. 2013), and *Euclid* (Laureijs et al. 2011) missions, considering the large amount of human effort and interaction required for the compilation of the present catalogue, which could not be extended to the huge datasets of these missions.

**Acknowledgements.** The Saclay team acknowledges long term support from the Centre National d'Etudes Spatiales.

This research has made use of "Aladin sky atlas" developed at CDS, Strasbourg Observatory, France ((Bonnarel, F. et al. 2000) and (Boch & Fernique 2014)). The cross-matching has made use of the NASA/IPAC Extragalactic Database (NED), which is operated by the Jet Propulsion Laboratory, California Institute of Technology, under contract with the National Aeronautics and Space Administration.

The Pan-STARRS1 Surveys (PS1) and the PS1 public science archive have been made possible through contributions by the Institute for Astronomy, the University of Hawaii, the Pan-STARRS Project Office, the Max-Planck Society and its participating institutes, the Max Planck Institute for Astronomy, Heidelberg and the Max Planck Institute for Extraterrestrial Physics, Garching, The Johns Hopkins University, Durham University, the University of Edinburgh, the Queen's University Belfast, the Harvard-Smithsonian Center for Astrophysics, the Las Cumbres Observatory Global Telescope Network Incorporated, the National Central University of Taiwan, the Space Telescope Science Institute, the National Aeronautics and Space Administration under Grant No. NNX08AR22G issued through the Planetary Science Division of the NASA Science Mission Directorate, the National Science Foundation Grant No. AST-1238877, the University of Maryland, Eotvos Lorand University (ELTE), the Los Alamos National Laboratory, and the Gordon and Betty Moore Foundation.

Funding for the Sloan Digital Sky Survey IV has been provided by the Alfred P. Sloan Foundation, the U.S. Department of Energy Office of Science, and the Participating Institutions. SDSS acknowledges support and resources from the Center for High-Performance Computing at the University of Utah. The SDSS web site is [www.sdss.org](http://www.sdss.org).

SDSS is managed by the Astrophysical Research Consortium for the Participating Institutions of the SDSS Collaboration including the Brazilian Participation Group, the Carnegie Institution for Science, Carnegie Mellon University, Center for Astrophysics / Harvard & Smithsonian (CfA), the Chilean Participation Group, the French Participation Group, Instituto de Astrofísica de Canarias, The Johns Hopkins University, Kavli Institute for the Physics and Mathematics of the Universe (IPMU) / University of Tokyo, the Korean Participation Group, Lawrence Berkeley National Laboratory, Leibniz Institut für Astrophysik Potsdam (AIP), Max-Planck-Institut für Astronomie (MPIA Heidelberg), Max-Planck-Institut für Astrophysik (MPA Garching), Max-Planck-Institut für Extraterrestrische Physik (MPE), National Astronomical Observatories of China, New Mexico State University, New York University, University of Notre Dame, Observatório Nacional / MCTI, The Ohio State University, Pennsylvania State University, Shanghai Astronomical Observatory, United Kingdom Participation Group, Universidad Nacional Autónoma de México, University of Arizona, University of Colorado Boulder, University of Oxford, University of Portsmouth, University of Utah, University of Virginia, University of Washington, University of Wisconsin, Vanderbilt University, and Yale University.

The Legacy Surveys consist of three individual and complementary projects: the Dark Energy Camera Legacy Survey (DECaLS; NSF's OIR Lab Proposal ID 2014B-0404; PIs: David Schlegel and Arjun Dey), the Beijing-Arizona Sky Survey (BASS; NSF's OIR Lab Proposal ID 2015A-0801; PIs: Zhou Xu and Xiaohui Fan), and the Mayall z-band Legacy Survey (MzLS; NSF's OIR Lab Proposal ID 2016A-0453; PI: Arjun Dey). DECaLS, BASS and MzLS together include data obtained, respectively, at the Blanco telescope, Cerro Tololo Inter-American Observatory, The NSF's National Optical-Infrared Astronomy Research Laboratory (NSF's OIR Lab); the Bok telescope, Steward Observatory, University of Arizona; and the Mayall telescope, Kitt Peak National Observatory, NSF's OIR Lab. The Legacy Surveys project is honored to be permitted to conduct astronomical research on Iolkam Du'ag (Kitt Peak), a mountain with particular significance to the Tohono O'odham Nation.

The NSF's OIR Lab is operated by the Association of Universities for Research in Astronomy (AURA) under a cooperative agreement with the National Science Foundation.

This project used data obtained with the Dark Energy Camera (DECam), which was constructed by the Dark Energy Survey (DES) collaboration. Funding for the DES Projects has been provided by the U.S. Department of Energy, the U.S. National Science Foundation, the Ministry of Science and Education of Spain, the Science and Technology Facilities Council of the United Kingdom, the Higher Education Funding Council for England,

the National Center for Supercomputing Applications at the University of Illinois at Urbana-Champaign, the Kavli Institute of Cosmological Physics at the University of Chicago, Center for Cosmology and Astro-Particle Physics at the Ohio State University, the Mitchell Institute for Fundamental Physics and Astronomy at Texas A&M University, Financiadora de Estudos e Projetos, Fundacao Carlos Chagas Filho de Amparo, Financiadora de Estudos e Projetos, Fundacao Carlos Chagas Filho de Amparo a Pesquisa do Estado do Rio de Janeiro, Conselho Nacional de Desenvolvimento Cientifico e Tecnológico and the Ministerio da Ciencia, Tecnologia e Inovacao, the Deutsche Forschungsgemeinschaft and the Collaborating Institutions in the Dark Energy Survey. The Collaborating Institutions are Argonne National Laboratory, the University of California at Santa Cruz, the University of Cambridge, Centro de Investigaciones Energeticas, Medioambientales y Tecnologicas-Madrid, the University of Chicago, University College London, the DES-Brazil Consortium, the University of Edinburgh, the Eidgenössische Technische Hochschule (ETH) Zurich, Fermi National Accelerator Laboratory, the University of Illinois at Urbana-Champaign, the Institut de Ciències de l'Espai (IEEC/CSIC), the Institut de Física d'Altes Energies, Lawrence Berkeley National Laboratory, the Ludwig-Maximilians Universität München and the associated Excellence Cluster Universe, the University of Michigan, the National Optical Astronomy Observatory, the University of Nottingham, the Ohio State University, the University of Pennsylvania, the University of Portsmouth, SLAC National Accelerator Laboratory, Stanford University, the University of Sussex, and Texas A&M University.

BASS is a key project of the Telescope Access Program (TAP), which has been funded by the National Astronomical Observatories of China, the Chinese Academy of Sciences (the Strategic Priority Research Program "The Emergence of Cosmological Structures" Grant XDB09000000), and the Special Fund for Astronomy from the Ministry of Finance. The BASS is also supported by the External Cooperation Program of Chinese Academy of Sciences (Grant 114A11KYSB20160057), and Chinese National Natural Science Foundation (Grant 11433005).

The Legacy Survey team makes use of data products from the Near-Earth Object Wide-field Infrared Survey Explorer (NEOWISE), which is a project of the Jet Propulsion Laboratory/California Institute of Technology. NEOWISE is funded by the National Aeronautics and Space Administration.

The Legacy Surveys imaging of the DESI footprint is supported by the Director, Office of Science, Office of High Energy Physics of the U.S. Department of Energy under Contract No. DE-AC02-05CH1123, by the National Energy Research Scientific Computing Center, a DOE Office of Science User Facility under the same contract; and by the U.S. National Science Foundation, Division of Astronomical Sciences under Contract No. AST-0950945 to NOAO.

## References

- Adami, C., Giles, P., Koulouridis, E., et al. 2018, *A&A*, 620, A5
- Andreon, S., Serra, A. L., Moretti, A., & Trinchieri, G. 2016, *A&A*, 585, A147
- Benson, B. A., de Haan, T., Dudley, J. P., et al. 2013, *ApJ*, 763, 147
- Bertin, E. & Arnouts, S. 1996, *A&AS*, 117, 393
- Blanton, M. R., Bershad, M. A., Abolfathi, B., et al. 2017, *AJ*, 154, 28
- Boch, T. & Fernique, P. 2014, in *Astronomical Society of the Pacific Conference Series*, Vol. 485, *Astronomical Data Analysis Software and Systems XXIII*, ed. N. Manset & P. Forshay, 277
- Böhringer, H., Chon, G., & Collins, C. A. 2014, *A&A*, 570, A31
- Böhringer, H., Schuecker, P., Guzzo, L., et al. 2001, *A&A*, 369, 826
- Böhringer, H., Voges, W., Huchra, J. P., et al. 2000, *ApJS*, 129, 435
- Bonnarel, F., Fernique, P., Bienaymé, O., et al. 2000, *Astron. Astrophys. Suppl. Ser.*, 143, 33
- Cavaliere, A. & Fusco-Femiano, R. 1978, *A&A*, 70, 677
- Clerc, N., Adami, C., Lieu, M., et al. 2014, *MNRAS*, 444, 2723
- Clerc, N., Kirkpatrick, C. C., Finoguenov, A., et al. 2020, *MNRAS*, 497, 3976
- Clerc, N., Merloni, A., Zhang, Y. Y., et al. 2016, *MNRAS*, 463, 4490
- Clerc, N., Sadibekova, T., Pierre, M., et al. 2012, *MNRAS*, 423, 3561
- Comparat, J., Merloni, A., Dwelly, T., et al. 2020, *A&A*, 636, A97
- Dey, A., Schlegel, D. J., Lang, D., et al. 2019, *AJ*, 157, 168
- Dwelly, T., Salvato, M., Merloni, A., et al. 2017, *MNRAS*, 469, 1065
- Ebeling, H., Edge, A. C., & Henry, J. P. 2001, *ApJ*, 553, 668
- Faccioli, L., Pacaud, F., Sauvageot, J. L., et al. 2018, *A&A*, 620, A9
- Fassbender, R., Böhringer, H., Nastasi, A., et al. 2011, *New Journal of Physics*, 13, 125014
- Finoguenov, A., Guzzo, L., Hasinger, G., et al. 2007, *ApJS*, 172, 182
- Finoguenov, A., Rykoff, E., Clerc, N., et al. 2020, *A&A*, 638, A114
- Flewelling, H. A., Magnier, E. A., Chambers, K. C., et al. 2020, *ApJS*, 251, 7
- Frenk, C. S., White, S. D. M., Efstathiou, G., & Davis, M. 1990, *ApJ*, 351, 10
- Gioia, I. M., Maccacaro, T., Schild, R. E., et al. 1990, *ApJS*, 72, 567
- Gunn, J. E., Siegmund, W. A., Mannery, E. J., et al. 2006, *AJ*, 131, 2332
- Henry, J. P., Gioia, I. M., Maccacaro, T., et al. 1992, *ApJ*, 386, 408
- Henry, J. P., Mullis, C. R., Voges, W., et al. 2006, *ApJS*, 162, 304
- Kirkpatrick, C. C., Clerc, N., Finoguenov, A., et al. 2021, *arXiv e-prints*, arXiv:2101.04695
- Kosiba, M., Lieu, M., Altieri, B., et al. 2020, *MNRAS*, 496, 4141
- Laureijs, R., Amiaux, J., Arduini, S., et al. 2011, *arXiv e-prints*, arXiv:1110.3193
- Mantz, A., Allen, S. W., Rapetti, D., & Ebeling, H. 2010, *MNRAS*, 406, 1759
- Mantz, A. B., Abdulla, Z., Allen, S. W., et al. 2018, *A&A*, 620, A2
- Marconi, A. & Hunt, L. K. 2003, *ApJ*, 589, L21
- Mehrtens, N., Romer, A. K., Hilton, M., et al. 2012, *MNRAS*, 423, 1024
- Merloni, A., Predehl, P., Becker, W., et al. 2012, *arXiv e-prints*, arXiv:1209.3114
- Nandra, K., Barret, D., Barcons, X., et al. 2013, *arXiv e-prints*, arXiv:1306.2307
- O'Sullivan, E., Ponman, T. J., Kolokythas, K., et al. 2017, *MNRAS*, 472, 1482
- Pacaud, F., Pierre, M., Refregier, A., et al. 2006, *MNRAS*, 372, 578
- Piccinotti, G., Mushotzky, R. F., Boldt, E. A., et al. 1982, *ApJ*, 253, 485
- Pierre, M., Chiappetti, L., Pacaud, F., et al. 2007, *MNRAS*, 382, 279
- Pierre, M., Pacaud, F., Adami, C., et al. 2016, *A&A*, 592, A1
- Pierre, M., Valtchanov, I., Altieri, B., et al. 2004, *J. Cosmology Astropart. Phys.*, 9, 011
- Piffaretti, R., Arnaud, M., Pratt, G. W., Pointecouteau, E., & Melin, J. B. 2011, *A&A*, 534, A109
- Planck Collaboration, Ade, P. A. R., Aghanim, N., et al. 2014, *A&A*, 571, A20
- Plonies, M., López-Cruz, O., & Hughes, D. 2008, *A Pan-Chromatic View of Clusters of Galaxies and the Large-Scale Structure*, Vol. 740
- Predehl, P., Andritschke, R., Arefiev, V., et al. 2021, *A&A*, 647, A1
- Ramos-Ceja, M. E., Pacaud, F., Reiprich, T. H., et al. 2019, *A&A*, 626, A48
- Reblinski, K. & Bartelmann, M. 1999, *A&A*, 345, 1
- Ridl, J., Clerc, N., Sadibekova, T., et al. 2017, *MNRAS*, 468, 662
- Romer, A. K., Viana, P. T. P., Liddle, A. R., & Mann, R. G. 2001, *ApJ*, 547, 594
- Rozo, E., Wechsler, R. H., Rykoff, E. S., et al. 2010, *ApJ*, 708, 645
- Rykoff, E. S., Rozo, E., Busha, M. T., et al. 2014, *ApJ*, 785, 104
- Sadibekova, T., Pierre, M., Clerc, N., et al. 2014, *A&A*, 571, A87
- Salvato, M., Buchner, J., Budavári, T., et al. 2018, *MNRAS*, 473, 4937
- Santos, J. S., Fassbender, R., Nastasi, A., et al. 2011, *A&A*, 531, L15
- Scoville, N., Aussel, H., Brusa, M., et al. 2007, *ApJS*, 172, 1
- Sehgal, N., Trac, H., Acquaviva, V., et al. 2011, *ApJ*, 732, 44
- Starck, J. L. & Pierre, M. 1998, *A&AS*, 128, 397
- Takey, A., Durret, F., Mahmoud, E., & Ali, G. B. 2016, *A&A*, 594, A32
- Takey, A., Schwöpe, A., & Lamer, G. 2011, *A&A*, 534, A120
- Takey, A., Schwöpe, A., & Lamer, G. 2013, *A&A*, 558, A75
- Takey, A., Schwöpe, A., & Lamer, G. 2014, *A&A*, 564, A54
- van Haarlem, M. P., Frenk, C. S., & White, S. D. M. 1997, *MNRAS*, 287, 817
- Vikhlinin, A., Burenin, R. A., Ebeling, H., et al. 2009, *ApJ*, 692, 1033
- Šuhada, R., Song, J., Böhringer, H., et al. 2012, *A&A*, 537, A39
- Webb, N. A., Coriat, M., Traulsen, I., et al. 2020, *A&A*, 641, A136
- Willis, J. P., Clerc, N., Bremer, M. N., et al. 2013, *MNRAS*, 430, 134
- Wright, E. L., Eisenhardt, P. R. M., Mainzer, A. K., et al. 2010, *AJ*, 140, 1868

## Appendix A: Convolutional neural network classification of the provisional sources.

Convolutional neural networks (CNNs) are state-of-the-art machine-learning tools for image classification. In Kosiba et al. (2020), our team developed a custom CNN architecture for automatic classification of galaxy cluster candidates into two classes, 'galaxy cluster' and 'non-cluster'. To train the network, we provided it with X-ray and optical images of approximately 1500 galaxy cluster candidates together with their manual classifications as given by experts from the X-CLASS collaboration. The network used those data to learn how to understand patterns of different classes of objects and projection and instrumental effects of the data. When successfully trained, we evaluated the performance of the network on a sample of 85 spectroscopically confirmed galaxy clusters and 85 objects we classified as non-clusters. Our network achieved  $\sim 90\%$  accuracy. For more technical details on the construction of the data and our CNN architecture, we kindly refer the interested reader to Kosiba et al. (2020).

Here, we compare the CNN classifications with the expert opinions on the 225 'provisional' sources as described in Sect. 4.1.2. The results are illustrated in Fig. A.1. Mixed expert opin-

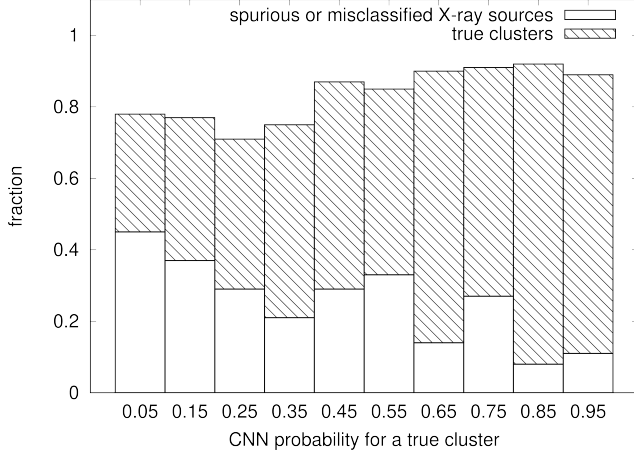


**Fig. A.1.** Agreement between CNN classification and expert opinion. The hatched area shows the fraction of sources agreed upon by all researchers as being true clusters, while the empty area shows the false detections agreed upon by all researchers. The percentage of sources for which the expert opinions are mixed is omitted for clarity, but these sources account for the remaining fraction up to 1 for each bin. The number of sources in each bin varies from 10 to 33. CNNs are shown to be more effective in identifying true clusters in the last two bins (CNN prob. > 80%) and false detections in the first bin (CNN prob. < 10%).

ions are not included in the histogram but they can easily be inferred as the remaining percentage in each bin. We clearly see that the CNN method is most successful in classifying sources as clusters with more than 80% probability (the last two bins). The agreement in both these bins is  $\sim 80\%$ . We conclude that, as expected, automatic classification of X-ray sources is more efficient at identifying true bonafide clusters than at discarding spurious or misclassified ones.

We stress that the CNN was not trained on provisional sources because these could not be labelled as ‘galaxy clusters’ or ‘non-clusters’ by definition of this class. The provisional sources are galaxy cluster candidates that the experts were not sure how to classify in the first manual screening, making them the hardest-to-classify galaxy cluster candidates.

However, further training of our CNN on a large sample of difficult cases with known true classification (e.g. spectroscopic confirmation) would make it more reliable for classification of difficult provisional sources and especially useful for large-area surveys where human interaction will be impossible.

## Appendix B: Detected sources on observed fields with less than three detectors

In this section, we provide a table of the additional nine X-ray extended sources that were detected on observations with one or two missing detectors.

**Table B.1.** X-ray clusters detected on XMM-Newton observations with less than three detectors. Redshift and status as defined in Sect. 5.1

RA (deg.)	Dec (deg.)	redshift	status	available detectors
7.436	4.873	0.206	confirmed	MOS1+MOS2
8.664	-12.12	0.44	photometric	MOS1+MOS2
110.22	71.151	0.231	confirmed	MOS1+MOS2
131.797	34.813	0.552	confirmed	MOS1+MOS2
154.798	45.047	–	–	MOS1+MOS2
155.151	45.005	–	provisional	MOS1+MOS2
175.353	-12.279	0.115	tentative	MOS1+MOS2
226.499	1.697	0.237	tentative	PN
156.059	4.193	–	provisional	PN

## Appendix C: X-CLASS clusters spectroscopically confirmed with SPIDERS

In Table C.1 we present the subsample of 124 clusters selected for spectroscopic follow-up within the frame of SPIDERS (see Sect. 4.1.3).

**Table C.1.** X-CLASS clusters spectroscopically confirmed with SPIDERS (see Sect. 4.1.3). This table lists the systems that are validated with  $N_{\text{mem}}$  spectroscopic redshifts selected among  $N_z$  redshifts available in their red sequence. The observational status indicates ‘complete’ if all selected targets led to a spectrum acquisition. The spectroscopic redshift uncertainty reflects the spread in the  $N_{\text{mem}}$  redshift values. A few systems marked with <sup>(1)</sup> were confirmed with only two spectroscopic members, hence no uncertainty is given on the redshift.

Xclass	$N_z$	Obs. status	$N_{\text{mem}}$	Zspec	Xclass	$N_z$	Obs. status	$N_{\text{mem}}$	Zspec
0039	12	complete	7	$0.2810 \pm 0.0009$	1624	15	complete	12	$0.2276 \pm 0.0009$
0040	15	complete	12	$0.3274 \pm 0.0009$	1626	5	complete	5	$0.548 \pm 0.002$
0062	18	complete	18	$0.362 \pm 0.002$	1627	16	complete	15	$0.3297 \pm 0.0009$
0096	17	complete	16	$0.252 \pm 0.001$	1635	11	complete	8	$0.428 \pm 0.001$
0099	26	complete	22	$0.2311 \pm 0.0007$	1637	24	complete	22	$0.206 \pm 0.001$
0102	15	complete	14	$0.0593 \pm 0.0003$	1642	14	complete	9	$0.55 \pm 0.01$
0103	12	complete	11	$0.1320 \pm 0.0005$	1674	17	complete	8	$0.580 \pm 0.001$
0108	19	complete	14	$0.1949 \pm 0.0006$	1676	27	complete	14	$0.2881 \pm 0.0004$
0109	12	complete	9	$0.478 \pm 0.001$	1678	24	complete	18	$0.409 \pm 0.002$
0110	24	complete	14	$0.2703 \pm 0.0009$	1680	4	complete	3	$0.552 \pm 0.004$
0169	10	complete	9	$0.320 \pm 0.002$	1686	11	complete	6	$0.3076 \pm 0.0009$
0224	15	complete	11	$0.1423 \pm 0.0006$	1706	9	incomplete	6	$0.3321 \pm 0.0004$
0245	10	complete	7	$0.1603 \pm 0.0003$	1737	21	complete	20	$0.276 \pm 0.001$
0270	15	complete	12	$0.2452 \pm 0.0006$	1738	20	complete	18	$0.280 \pm 0.002$
0336	17	complete	13	$0.421 \pm 0.001$	1758	7	complete	6	$0.342 \pm 0.001$
0342	4	incomplete	3	$0.230 \pm 0.003$	1763	9	complete	4	$0.3124 \pm 0.0006$
0343	17	incomplete	15	$0.351 \pm 0.001$	1764	15	complete	8	$0.311 \pm 0.001$
0344	14	complete	11	$0.2909 \pm 0.0006$	1789	10	complete	2	$0.59^{(1)}$
0347	3	incomplete	2	$0.26^{(1)}$	1807	16	complete	10	$0.4999 \pm 0.0006$
0349	28	complete	22	$0.1537 \pm 0.0005$	1816	10	complete	3	$0.579 \pm 0.001$
0361	8	complete	7	$0.0454 \pm 0.0007$	1817	9	complete	5	$0.579 \pm 0.002$
0377	9	incomplete	8	$0.395 \pm 0.002$	1853	33	complete	26	$0.2972 \pm 0.0008$
0574	8	complete	4	$0.497 \pm 0.002$	1854	14	complete	8	$0.519 \pm 0.001$
0578	30	complete	29	$0.1396 \pm 0.0007$	1855	11	complete	8	$0.1865 \pm 0.0007$
0615	11	complete	6	$0.255 \pm 0.001$	1866	2	complete	2	$0.44^{(1)}$
0628	7	complete	6	$0.2323 \pm 0.0006$	1900	13	complete	8	$0.413 \pm 0.002$
0630	5	complete	4	$0.373 \pm 0.001$	1904	34	complete	32	$0.0895 \pm 0.0003$
0632	19	complete	14	$0.3947 \pm 0.0005$	1941	17	complete	14	$0.0996 \pm 0.0003$
0638	6	complete	4	$0.500 \pm 0.001$	1957	23	complete	23	$0.2696 \pm 0.0009$
0686	8	complete	4	$0.460 \pm 0.003$	1982	10	complete	6	$0.248 \pm 0.001$
0706	5	complete	4	$0.609 \pm 0.002$	1983	10	complete	9	$0.3453 \pm 0.0004$
0734	6	complete	4	$0.427 \pm 0.004$	2003	7	complete	5	$0.532 \pm 0.003$
0740	14	complete	9	$0.3388 \pm 0.0008$	2026	8	complete	4	$0.527 \pm 0.001$
0755	18	complete	14	$0.1969 \pm 0.0004$	2034	6	incomplete	5	$0.248 \pm 0.001$
0841	13	complete	7	$0.551 \pm 0.003$	2036	13	complete	6	$0.328 \pm 0.001$
0842	29	complete	22	$0.3009 \pm 0.0009$	2051	17	complete	9	$0.411 \pm 0.002$
0890	19	complete	13	$0.3397 \pm 0.0007$	2080	11	complete	6	$0.427 \pm 0.002$
0908	16	complete	11	$0.2744 \pm 0.0005$	2081	21	complete	19	$0.293 \pm 0.002$
0953	12	complete	7	$0.1327 \pm 0.0002$	2088	13	complete	11	$0.0900 \pm 0.0009$
0963	13	complete	12	$0.2477 \pm 0.0005$	2090	26	complete	25	$0.0904 \pm 0.0006$
1013	10	complete	8	$0.4149 \pm 0.0005$	2093	21	complete	16	$0.2970 \pm 0.0008$
1059	26	complete	22	$0.2791 \pm 0.0005$	2097	19	complete	18	$0.1125 \pm 0.0006$
1062	26	complete	22	$0.1238 \pm 0.0004$	2109	25	complete	20	$0.2128 \pm 0.0006$
1069	9	complete	9	$0.1328 \pm 0.0004$	2154	8	complete	7	$0.329 \pm 0.001$
1086	7	complete	7	$0.423 \pm 0.002$	2155	9	complete	8	$0.390 \pm 0.001$
1159	22	complete	20	$0.412 \pm 0.001$	2182	6	complete	6	$0.520 \pm 0.002$
1185	11	complete	5	$0.492 \pm 0.002$	2208	13	complete	8	$0.1050 \pm 0.0004$
1288	18	complete	13	$0.532 \pm 0.002$	2214	20	complete	15	$0.3004 \pm 0.0004$
1307	28	complete	26	$0.0593 \pm 0.0004$	2272	13	complete	9	$0.254 \pm 0.003$
1350	4	incomplete	3	$0.396 \pm 0.001$	2295	28	complete	22	$0.3695 \pm 0.0007$
1351	11	incomplete	6	$0.543 \pm 0.002$	2328	2	complete	2	$0.45^{(1)}$
1368	23	complete	20	$0.288 \pm 0.001$	2338	31	complete	29	$0.1406 \pm 0.0004$
1369	12	complete	5	$0.284 \pm 0.002$	2340	12	complete	11	$0.443 \pm 0.002$
1386	13	complete	12	$0.314 \pm 0.001$	2344	21	complete	21	$0.232 \pm 0.002$
1439	23	complete	21	$0.0573 \pm 0.0006$	2345	22	complete	20	$0.219 \pm 0.001$
1443	31	complete	24	$0.0543 \pm 0.0006$	2347	28	complete	26	$0.1672 \pm 0.0007$
1451	8	complete	6	$0.478 \pm 0.004$	2348	26	complete	25	$0.1921 \pm 0.0009$
1452	7	complete	5	$0.447 \pm 0.004$	2350	23	complete	20	$0.412 \pm 0.001$
1543	10	complete	10	$0.370 \pm 0.001$	2353	25	complete	23	$0.190 \pm 0.001$
1544	19	complete	18	$0.370 \pm 0.001$	2358	30	complete	25	$0.0949 \pm 0.0007$
1548	5	complete	5	$0.3281 \pm 0.0006$	2360	14	complete	10	$0.235 \pm 0.002$
1622	21	complete	14	$0.0794 \pm 0.0003$	2363	14	complete	8	$0.312 \pm 0.002$

**Appendix D: Provisional sources**

Table D.1 presents the subsample of 87 candidate clusters for which the visual screening (see Sect. 4.1.2) did not provide a conclusive result. These sources are not included in the online public catalogue.

**Table D.1.** X-CLASS clusters classified as ‘provisional’.

Xclass	RA (deg.)	Dec (deg.)	total rate (counts/sec)	Xclass	RA (deg.)	Dec (deg.)	total rate (counts/sec)
20070	0.792	-29.968	0.05688	3424	169.214	17.987	0.03811
0489	11.785	25.278	3.66885	1894	169.572	7.971	0.01281
0486	11.858	-25.126	0.03257	0231	172.902	-34.695	0.02231
0508	16.507	-80.151	0.03299	2268	178.981	23.403	0.01315
0889	20.281	3.826	0.01776	22889	180.352	-18.832	0.01657
3146	23.316	30.746	0.04004	21578	184.771	5.819	0.02551
20173	32.009	35.463	0.02230	23494	186.144	7.186	0.01566
20828	32.556	-0.198	0.03283	3390	186.307	12.662	0.12703
1850	34.570	-73.938	0.03450	21781	188.338	70.765	0.04260
21766	34.963	-6.148	0.01781	0497	188.965	12.498	0.01774
3378	37.592	-60.554	0.15114	2105	194.340	26.898	0.01816
3020	40.277	-8.315	0.01193	2103	194.450	27.402	0.04238
3334	40.876	32.421	0.30850	0560	195.646	-2.307	0.02117
3093	50.413	-37.128	0.03664	21170	197.706	57.658	0.05172
2426	50.602	-37.160	0.08201	23576	198.539	-16.381	0.03641
20052	54.544	0.318	0.03535	0447	201.280	-38.507	0.34308
3398	55.118	-18.574	0.02939	1359	202.274	58.447	0.02694
1709	56.078	24.589	0.01932	20318	203.157	-31.798	0.07504
22693	58.565	-59.036	0.01911	20177	204.294	51.931	0.03124
20953	61.904	-12.364	0.03154	0406	209.029	18.395	0.06527
2502	62.600	-75.231	0.02606	0071	211.053	-33.858	0.05082
1981	63.084	-28.533	0.01731	3368	211.633	25.134	0.00993
2343	68.093	-13.263	0.03117	3369	211.732	25.011	0.01606
1292	72.174	-66.052	0.04434	3113	213.205	-34.298	0.02489
3116	73.702	-10.254	0.02499	1766	213.722	36.205	0.08474
2288	83.290	-62.426	0.01029	20700	222.450	8.906	0.03159
23586	86.227	-25.738	0.01752	2372	227.778	70.718	0.04958
21432	117.482	55.862	0.03641	0907	233.187	32.712	0.01681
1930	122.110	-76.477	0.01407	22703	251.264	57.630	0.03171
3305	122.209	20.932	0.02117	3193	251.927	34.955	0.06984
3457	139.828	-11.985	0.01521	24820	260.420	57.876	0.02510
1618	144.532	71.116	0.01495	3165	262.827	6.031	0.01854
3085	145.470	46.854	0.02163	0204	314.015	-4.524	0.01769
1679	145.594	46.982	0.01284	1823	322.931	-42.876	0.02355
1777	146.697	9.805	0.26240	24447	324.265	-63.133	0.03605
21197	149.694	2.264	0.03038	21444	330.691	18.841	0.02231
2316	152.129	12.202	0.01674	2844	333.578	-10.265	0.03685
0434	156.059	4.192	0.00467	21706	334.159	-36.817	0.03245
24309	161.450	4.364	0.08199	22786	339.026	34.182	0.02820
23209	162.955	57.546	0.01016	2052	344.267	-43.337	0.03379
22477	163.180	10.547	0.01799	2159	349.022	-2.428	0.04161
0813	163.192	57.355	0.01775	1911	349.555	-42.193	0.05136
22475	163.281	10.707	0.03708	21587	352.266	14.865	0.04891
3060	164.630	1.634	0.02172				